

# **THEORETICAL AND APPLIED RESEARCH IN NATURAL SCIENCES AND MATHEMATICS**

---

**Editor**  
**Prof. Dr. Şifa TÜRKOĞLU**



**THEORETICAL AND  
APPLIED RESEARCH IN  
NATURAL SCIENCES AND  
MATHEMATICS**

**Editor**  
**Prof. Dr. Şifa TÜRKOĞLU**



*Theoretical And Applied Research In Natural Sciences And Mathematics*

*Editor: Prof. Dr. Şifa TÜRKOĞLU*

**Editor in chief:** Berkan Balpetek

**Cover and Page Design:** Duvar Design

**Printing :** October -2025

**Publisher Certificate No:** 49837

**ISBN:** 978-625-8734-08-9

© Duvar Yayınları

853 Sokak No:13 P.10 Kemeraltı-Konak/İzmir

Tel: 0 232 484 88 68

[www.duvar yayinlari.com](http://www.duvar yayinlari.com)

[duvarkitabevi@gmail.com](mailto:duvarkitabevi@gmail.com)

*The authors bear full responsibility for the sources, opinions, findings, results, tables, figures, images, and all other content presented in the chapters of this book. They are solely accountable for any financial or legal obligations that may arise in connection with national or international copyright regulations. The publisher and editors shall not be held liable under any circumstances*

## TABLE OF CONTENTS

### Chapter 1 .....1

Three-Moment Chi-Square Approximation for the Distributions of  
Modified Levene Tests  
*Gamze GÜVEN, Birdal ŞENOĞLU*

### Chapter 2 .....20

Photodetection and Solar Energy Harvesting  
Using Schottky Junctions  
*İlhan CANDAN, Sezai ASUBAY*

### Chapter 3 .....35

Performance Evaluation of Numerical Root Finding Methods Using  
Fibonacci and Golden Ratio Algorithms  
*Bayram KÖSE, Bahar DEMİRTÜRK, Şükran KONCA*

### Chapter 4 .....52

A Savings Model under Nonlocal Boundary Conditions  
*Olgun CABRİ, Hanlar REŞİDOĞLU*

### Chapter 5.....63

Kamada-Kawai Algorithm: A Comprehensive Analysis from  
Global Graph Layout to Modern Challenges  
*Ümit SARP, Bilal DEMİR*

## Three-Moment Chi-Square Approximation for the Distributions of Modified Levene Tests

Gamze GÜVEN<sup>1</sup>, Birdal ŞENOĞLU<sup>2</sup>

### 1 Introduction

The problem of testing homogeneity of variances has been the primary concern of researchers and practitioners for decades. Because some statistical procedures such as the Student's  $t$ -test and the ANOVA  $F$ -test are sensitive to violations of the homoscedasticity assumption, verifying the homogeneity of variances is one of the initial steps in practice across many areas, including economics, health sciences, and engineering, see Ederington and Lee (1993), Li et al. (1997), Li et. al (2015), Esi and Baykal (2020), Zhou et al. (2023) and references therein for detailed information.

There are numerous studies in literature for testing homogeneity of variances of  $k$  independent groups. The hypothesis of interest is

$$H_0: \sigma_1^2 = \sigma_2^2 = \dots = \sigma_k^2 \quad (1)$$

against the alternative hypothesis  $H_1: \sigma_i^2 \neq \sigma_j^2$  for at least one  $i \neq j$ .

In this context, Bartlett (1937) introduced one of the earliest procedures, a modified likelihood ratio test that is the most powerful when the normality assumption holds. Levene (1960) proposed a test for equality of variances, initially developed for equal sample sizes and later generalized to unbalanced designs. This test performs a one-way ANOVA on modified data, where each observation is replaced by its absolute deviation from its group mean. Layard (1973) discussed two asymptotically robust tests, a simple chi-square test and a test based on jackknife procedure. Brown and Forsythe (1974) referred to Levene's original test as  $W_0$  and proposed two modified versions of it by replacing the group mean with the 10% trimmed mean and the median, which were denoted as  $W_{10}$  and  $W_{50}$ , respectively. Simulation results reported by Brown

---

<sup>1</sup> Assoc. Prof., Eskisehir Osmangazi University, ORCID:0000-0002-8821-3179, gamzeguven@ogu.edu.tr

<sup>2</sup> Prof., Ankara University, ORCID: 0000-0003-3707-2393, senoglu@science.ankara.edu.tr

and Forsythe (1974) indicated that  $W_{50}$  tends to be conservative for small sample sizes under normality, whereas  $W_{10}$  exhibits greater robustness when the underlying distributions are long tailed. Lim and Loh (1996) compared  $W_{50}$  test, Bartlett test with and without kurtosis adjustment, Box-Anderson test, three jackknife tests and their bootstrap counterparts in terms of robustness and power. They concluded that  $W_{50}$  test and its bootstrap version, along with one jackknife test and the kurtosis-adjusted Bartlett test, exhibit desirable robustness and power properties. Sharma (1991) proposed a new jackknife test based on jackknifing one group of observations at a time, while Sarkar et al. (1999) modified Levene's test using the weighted likelihood estimates of the population means. Cahoy (2010) developed a bootstrap procedure based on variance-derived statistics. More recently, Sharma and Kibria (2013) compared 25 different test procedures under various conditions. Jayalath et al. (2017) introduced a bootstrap test based on the ratio of mean absolute deviances and developed a two-stage approach that first measures skewness to determine the suitable test for variance homogeneity. Esmailzadeh (2019) compared five Levene-type tests in terms of power and size.

Although no single test for homogeneity of variances achieves uniform superiority across scenarios studied in literature, Bartlett's, Levene's, and particularly the variants of Levene's procedure  $W_{10}$  and  $W_{50}$  are among the most widely used tests in applied sciences. As mentioned earlier, the  $W_{10}$  is obtained by performing a one-way ANOVA on the absolute deviations from each group's 10% trimmed mean, whereas  $W_{50}$  is defined analogously using the group median. Under normality, Bartlett's test is the most powerful but is sensitive to the departures from normality. In contrast,  $W_{10}$  and  $W_{50}$  tests maintain better control of Type I error rates in the presence of non-normal data, though their power may be low for some distributions and sample size configurations, see Conover et al. (1981) and Jayalath et al. (2017).

Motivated by their prevalent usage in applications, computational simplicity, and robustness to departures from normality, we focus on the  $W_{10}$  and  $W_{50}$  tests in this study. For both procedures, the usual one-way ANOVA  $F$ -ratio is computed on absolute deviations;  $p$ -values are obtained from the  $F$  reference distribution with  $(k - 1, N - k)$  degrees of freedom, and  $H_0$  in (1) is rejected when the observed statistic exceeds the corresponding critical value. However,  $W_{10}$  and  $W_{50}$  tests may fail to control the Type I error adequately in certain distributional settings, especially for small samples. Inspired by Tiku (1965), we approximate the null distributions of the  $W_{10}$  and  $W_{50}$  test statistics using the three-moment chi-square approximation, thereby overcoming this limitation. In their study, approximation was applied to the distributions of the Watson's  $U_N^2$

and Anderson-Darling's  $W_N^2$  statistics and resulting upper-tail percentage points were shown to agree closely with those reported by Stephens (1964). Tiku and Wong (1998) developed three-moment chi-square and four-moment F approximations for unit-root testing in AR (1) models when the underlying distributions are symmetric. Sürücü and Sazak (2009) provided two-moment normal and three-moment chi-square approximations for distribution of the sum of independent Weibull random variates and showed that they are accurate and useful for detecting production stabilities. Güven (2023) used three-moment chi-square and four-moment F approximations for the null distributions of Cochran's (1937) test and its robust version.

The remainder of the paper is organized as follows. Section 2 briefly reviews Bartlett's test, Levene's test, and the  $W_{10}$  and  $W_{50}$  tests. Section 3 describes a three-moment chi-square approximation for the null distributions of the  $W_{10}$  and  $W_{50}$  statistics. Section 4 conducts a Monte Carlo simulation study to evaluate the simulated Type I error rate and power for  $W_{10}$ ,  $W_{50}$ , and their moment-matched counterparts under different distributions and sample size configurations. Section 5 presents concluding remarks.

## 2 Descriptions of the Tests

In this section, the Bartlett, Levene,  $W_{10}$  and  $W_{50}$  tests for testing the homogeneity of variances are briefly described. Let  $X_{i1}, X_{i2}, \dots, X_{in_i}$  ( $i = 1, 2, \dots, k; j = 1, 2, \dots, n_i$ ) be independent random samples of size  $n_i$  drawn from  $k$  normal groups, each with variance  $\sigma_i^2$ . Define the sample mean and variance of the  $i$ th group as  $\bar{X}_i$  and  $S_i^2 = \frac{\sum_{j=1}^{n_i} (X_{ij} - \bar{X}_i)^2}{n_i - 1}$ , respectively. Also, total sample size is  $N = \sum_{i=1}^k n_i$ .

**Bartlett's Test:** Bartlett's test statistics is defined as

$$BT = \frac{(N-k) \ln S_a^2 - \sum_{i=1}^k (n_i - 1) \ln S_i^2}{1+C}$$

where

$$S_a^2 = \frac{\sum_{i=1}^k (n_i - 1) S_i^2}{N - k}$$

and the correction factor

$$C = \frac{1}{3(k-1)} \left( \sum_{i=1}^k \frac{1}{n_i - 1} - \frac{1}{N - k} \right).$$

The null hypothesis in (1) is rejected when

$$BT > \chi_{1-\alpha}^2(k-1),$$

where  $\chi_{1-\alpha}^2(k-1)$  denotes the  $100(1-\alpha)$ th percentile of the  $\chi^2$  distribution with  $(k-1)$  degrees of freedom.

It is well known, however, that Bartlett's test is highly sensitive to departures from normality.

**Levene's Test:** Levene's test is defined as

$$W_0 = \frac{(N-k) \sum_{i=1}^k n_i (\bar{z}_{i\cdot} - \bar{z}_{\cdot\cdot})^2}{(k-1) \sum_{i=1}^k \sum_{j=1}^{n_i} (z_{ij} - \bar{z}_{i\cdot})^2},$$

where

$$z_{ij} = |X_{ij} - \bar{X}_i|, \quad \bar{z}_{i\cdot} = \sum_{j=1}^{n_i} z_{ij} / n_i \quad \text{and} \quad \bar{z}_{\cdot\cdot} = \sum_{i=1}^k \sum_{j=1}^{n_i} z_{ij} / N.$$

The null hypothesis is rejected when

$$W_0 > F_{1-\alpha}(k-1, N-k),$$

where  $F_{1-\alpha}(k-1, N-k)$  denotes the  $100(1-\alpha)$ th percentile of the  $F$ -distribution with  $(k-1)$  and  $(N-k)$  degrees of freedom.

**$W_{10}$  Test:** Brown and Forsythe (1974) revised Levene's test by using trimmed mean rather than sample mean as follows

$$W_{10} = \frac{(N-k) \sum_{i=1}^k n_i (\bar{z}_{i\cdot} - \bar{z}_{\cdot\cdot})^2}{(k-1) \sum_{i=1}^k \sum_{j=1}^{n_i} (z_{ij} - \bar{z}_{i\cdot})^2},$$

where

$$z_{ij} = |X_{ij} - \tilde{X}_{i(10)}|, \quad \bar{z}_{i\cdot} = \sum_{j=1}^{n_i} z_{ij} / n_i \quad \text{and} \quad \bar{z}_{\cdot\cdot} = \sum_{i=1}^k \sum_{j=1}^{n_i} z_{ij} / N.$$

Here,  $\tilde{X}_{i(10)}$  denotes the 10% trimmed mean of the  $i$ th group.

The null hypothesis in (1) is rejected when

$$W_{10} > F_{1-\alpha}(k-1, N-k),$$

where  $F_{1-\alpha}(k-1, N-k)$  denotes the  $100(1-\alpha)$ th percentile of the  $F$ -distribution with  $(k-1)$  and  $(N-k)$  degrees of freedom.

**$W_{50}$  Test:** Brown and Forsythe (1974) also proposed the  $W_{50}$  test, which replaces the group mean in Levene's test statistics with the group median. It is defined as

$$W_{50} = \frac{(N-k) \sum_{i=1}^k n_i (\bar{z}_{i\cdot} - \bar{z}_{\cdot\cdot})^2}{(k-1) \sum_{i=1}^k \sum_{j=1}^{n_i} (z_{ij} - \bar{z}_{i\cdot})^2},$$

where

$$z_{ij} = |X_{ij} - \tilde{X}_i|, \quad \bar{z}_{i\cdot} = \sum_{j=1}^{n_i} z_{ij}/n_i \quad \text{and} \quad \bar{z}_{\cdot\cdot} = \sum_{i=1}^k \sum_{j=1}^{n_i} z_{ij}/N.$$

Here,  $\tilde{X}_i$  denotes the median of the  $i$ th group.

The null hypothesis in (1) is rejected when

$$W_{50} > F_{1-\alpha}(k-1, N-k),$$

where  $F_{1-\alpha}(k-1, N-k)$  denotes the  $100(1-\alpha)$ th percentile of the  $F$ -distribution with  $(k-1)$  and  $(N-k)$  degrees of freedom.

**Remark:** Levene's test statistics is based on absolute deviations from the group mean. Transformed observations  $Z_{ij} = |X_{ij} - \bar{X}_i|$  are neither strictly independent within each group nor normally distributed, however Levene showed the correlation is of order  $1/n_i^2$ , so the resulting dependence has a negligible impact on the distribution of  $W_0$ . In addition, since the one-way ANOVA procedures control the Type I error rates for moderate departures from normality, Levene's method explicitly takes advantage of this fact. Consequently,  $W_0$  is approximated by an  $F$ -distribution with  $(k-1)$  and  $(N-k)$  degrees of freedom

under null hypothesis. In line with Levene's test,  $W_{10}$  and  $W_{50}$  tests use the same  $F$  reference distribution, see Elamir (2023), Gastwirth et. al (2009) and references therein.

### 3 Three Moment Chi-Square Approximation for $W_{10}$ and $W_{50}$ Statistics

Let  $W_T$  denote the statistics of interest and define

$$W_A^T = (W_T + a_T)/b_T \quad (2)$$

where  $T \in \{10, 50\}$ . Let  $\mu_1^{(T)}$  be the mean of  $W_T$  and  $\mu_2^{(T)}$ ,  $\mu_3^{(T)}$  and  $\mu_4^{(T)}$  be variance, third and fourth central moments of  $W_T$ , respectively. Define the Pearson coefficients

$$\beta_1^{*(T)} = \left(\mu_3^{(T)}\right)^2 / \left(\mu_2^{(T)}\right)^3 \text{ and } \beta_2^{*(T)} = \mu_4^{(T)} / \left(\mu_2^{(T)}\right)^2. \quad (3)$$

If the coefficients in (3) satisfy the condition

$$E_T = \left| \beta_2^{*(T)} - \left(3 + 1.5 \beta_1^{*(T)}\right) \right| \leq 0.5, \quad (4)$$

then, the distribution of  $W_A^T$  is central chi-square with  $\nu_T$  degrees of freedom.  $a_T$ ,  $b_T$ , and  $\nu_T$  are obtained by equating the first three moments of both sides of (2) as follows

$$\nu_T = 8/\beta_1^{*(T)}, \quad b_T = \sqrt{\mu_2^{(T)}/2\nu_T} \text{ and } a_T = b_T\nu_T - \mu_1^{(T)}. \quad (5)$$

Note that the line  $\beta_2^{*(T)} = \left(3 + 1.5 \beta_1^{*(T)}\right)$  is known as the Type III line, see for details Pearson (1959) and Tiku (1965). Realize that we refer to  $W_T$  as the statistics of interest and to  $W_A^T$  as its moment-matched chi-square counterpart.

### 4 Simulation Study

This section begins with a comparison of Type I error rates for  $W_{10}$ ,  $W_{50}$ ,  $W_A^{10}$  and  $W_A^{50}$ , followed by a power comparison between  $W_A^{10}$  and  $W_A^{50}$ . The data  $X_{ij}$ ,  $i = 1, 2, \dots, k$ ;  $j = 1, 2, \dots, n_i$  are generated from six different distributions designed to cover various tail thicknesses and degrees of asymmetry. In this study

- (a) Normal ( $\mu = 0, \sigma = 1$ ), (b) Uniform (0,1),  
(c) STS ( $r = 2, d = 0, \mu = 0, \sigma = 1$ ), (d) LTS ( $p = 3.5, \mu = 0, \sigma = 1$ ),  
(e)  $\chi^2_{\nu=5}$ , (f) Beta ( $a = 10, b = 2$ )

distributions are considered and the skewness and kurtosis values of them are given below, see Table 1.

Table 1. Skewness and kurtosis values for the distributions considered in the simulation study.

	(a)	(b)	(c)	(d)	(e)	(f)
<i>Skewness</i>	0	0	0	0	1.265	-0.921
<i>Kurtosis</i>	3	1.8	2.437	6	5.4	3.789

From Table 1 it is evident that the first four distributions are symmetric, while the last two are right-skewed and left-skewed, respectively. Detailed definitions and properties of the LTS and STS distributions proposed by Tiku and Kumra (1985) and Tiku and Vaughan (1999), respectively, are provided in the Appendix.

The simulation setup is organized as follows

Number of groups $k$	4
Sample sizes $(n_1, n_2, n_3, n_4)$	$(5,5,5,5), (10,10,10,10),$ $(5,7,9,11), (10,15,20,25)$

To estimate Type I error rates for  $W_T$  with  $T \in \{10, 50\}$ , we generate data under the null hypothesis of homoscedasticity and compute  $W_T$  then repeat this procedure for  $R = 10,000$  Monte Carlo replications. The Type I error rates for  $W_T$  is the proportion of replications in which  $W_T$  exceeds the  $F$  critical value with  $(k - 1, N - k)$  degrees of freedom.

Because the closed-form moments of  $W_T$  are analytically intractable, we estimate its first four moments from the simulated  $W_T$  values via 10,000 Monte Carlo replications. Using these estimates, we obtain  $E_T$  from Eq. (4) and  $\nu_T, b_T$ , and  $a_T$  from Eq. (5), yielding a single set of  $(E_T, \nu_T, b_T, a_T)$  for each  $T$ . We then compute corresponding  $W_A^T$  values using Eq. (2) based on  $(a_T, b_T)$  values for each of the 10,000 simulated  $W_T$  values. The Type I error rates for  $W_A^T$  is the proportion of replications in which  $W_A^T$  exceeds the chi-square critical value  $\chi^2_{1-\alpha}(\nu_T)$ . Equivalently, it is the proportion of replications in which  $W_T$  exceeds the back-transformed cutoff  $c_{\alpha,T} = b_T \chi^2_{1-\alpha}(\nu_T) - a_T$ . Tables 2 and 3 report

$\mu_1^{(T)}, \mu_2^{(T)}, \beta_1^{*(T)}, \beta_2^{*(T)}, E_T$ , and  $c_{\alpha,T}$  for the  $W_T$  statistics when  $T = 10$  and  $T = 50$ , respectively.

**Table 2.** Simulated values of  $\mu_1^{(10)}, \mu_2^{(10)}, \beta_1^{*(10)}, \beta_2^{*(10)}, E_{10}$  and  $c_{\alpha,10}$  for  $W_{10}$  statistics.

	$\mu_1^{(10)}$	$\mu_2^{(10)}$	$\beta_1^{*(10)}$	$\beta_2^{*(10)}$	$E_{10}$	$c_{\alpha,10}$
Sample sizes	Normal (0,1)					
(5,5,5,5)	1.442	1.812	5.704	11.940	0.384	4.149
(5,7,9,11)	1.251	1.176	3.862	8.635	0.158	3.413
(10,10,10,10)	1.125	0.949	3.633	8.479	0.029	3.063
(10,15,20,25)	1.112	0.888	3.274	8.183	0.272	2.980
	Uniform (0,1)					
(5,5,5,5)	1.426	2.145	6.359	2.644	0.106	4.373
(5,7,9,11)	1.237	1.285	4.340	9.494	0.016	3.504
(10,10,10,10)	1.108	0.937	3.463	8.056	0.138	3.031
(10,15,20,25)	1.128	0.964	3.226	7.636	0.203	3.072
	STS ( $r = 2, d = 0, \mu = 0, \sigma = 1$ )					
(5,5,5,5)	1.418	1.766	4.858	10.297	0.009	4.084
(5,7,9,11)	1.249	1.240	3.871	8.543	0.263	3.469
(10,10,10,10)	1.095	0.902	3.345	7.919	0.099	2.979
(10,15,20,25)	1.150	0.969	3.409	8.133	0.020	3.105
	LTS ( $p = 3.5, \mu = 0, \sigma = 1$ )					
(5,5,5,5)	1.605	2.060	5.309	11.380	0.415	4.489
(5,7,9,11)	1.360	1.323	3.936	9.376	0.472	3.654
(10,10,10,10)	1.131	0.887	3.097	7.700	0.055	2.994
(10,15,20,25)	1.119	0.846	3.140	7.691	0.019	2.940
	$\chi_5^2$					
(5,5,5,5)	1.966	3.487	7.454	14.665	0.485	5.721
(5,7,9,11)	1.680	2.394	5.686	11.988	0.459	4.792
(10,10,10,10)	1.301	1.285	3.932	9.053	0.156	3.562
(10,15,20,25)	1.327	1.314	3.970	9.307	0.353	3.614
	Beta (10, 2)					
(5,5,5,5)	1.803	3.023	7.448	14.606	0.434	5.300
(5,7,9,11)	1.516	1.818	4.483	9.958	0.234	4.216
(10,10,10,10)	1.279	1.247	3.971	9.296	0.339	3.507
(10,15,20,25)	1.250	1.126	3.307	7.982	0.021	3.354

**Table 3.** Simulated values of  $\mu_1^{(50)}, \mu_2^{(50)}, \beta_1^{*(50)}, \beta_2^{*(50)}, E_{50}$  and  $c_{\alpha,50}$  for  $W_{50}$  statistics.

	$\mu_1^{(50)}$	$\mu_2^{(10)}$	$\beta_1^{*(50)}$	$\beta_2^{*(50)}$	$E_{50}$	$c_{\alpha,50}$
Sample sizes	Normal (0,1)					
(5,5,5,5)	0.703	0.318	2.566	6.839	0.010	1.810
(5,7,9,11)	0.808	0.433	2.769	7.371	0.217	2.103
(10,10,10,10)	0.915	0.593	3.410	8.611	0.495	2.444
(10,15,20,25)	0.958	0.642	3.022	7.614	0.081	2.541
	Uniform (0,1)					
(5,5,5,5)	0.531	0.205	3.082	7.518	0.106	1.427
(5,7,9,11)	0.676	0.342	3.514	8.160	0.111	1.838
(10,10,10,10)	0.803	0.546	4.732	10.167	0.070	2.285
(10,15,20,25)	0.879	0.551	2.768	6.964	0.189	2.340
	STS ( $r = 2, d = 0, \mu = 0, \sigma = 1$ )					
(5,5,5,5)	0.623	0.272	3.101	7.454	0.198	1.656
(5,7,9,11)	0.774	0.392	2.665	7.423	0.426	2.005
(10,10,10,10)	0.882	0.619	3.935	8.847	0.055	2.452
(10,15,20,25)	0.931	0.603	3.152	8.071	0.344	2.468
	LTS ( $p = 3.5, \mu = 0, \sigma = 1$ )					
(5,5,5,5)	0.754	0.355	2.654	7.022	0.041	1.925
(5,7,9,11)	0.883	0.503	3.218	8.290	0.463	2.287
(10,10,10,10)	0.948	0.595	2.855	7.201	0.081	2.469
(10,15,20,25)	0.999	0.644	2.516	6.809	0.035	2.572
	$\chi_5^2$					
(5,5,5,5)	0.763	0.387	4.051	9.463	0.388	2.005
(5,7,9,11)	0.914	0.566	3.132	7.361	0.337	2.402
(10,10,10,10)	0.988	0.731	4.109	9.261	0.097	2.695
(10,15,20,25)	1.006	0.711	3.498	8.325	0.078	2.681
	Beta (10, 2)					
(5,5,5,5)	0.724	0.343	3.055	7.701	0.119	1.882
(5,7,9,11)	0.872	0.518	3.270	8.167	0.262	2.298
(10,10,10,10)	0.983	0.766	4.740	10.520	0.409	2.738
(10,15,20,25)	0.989	0.688	3.206	7.956	0.148	2.631

It can be seen from Tables 2 and 3 that the condition  $E_T \leq 0.5$  in (4) is satisfied in all settings for  $T \in \{10, 50\}$ . Therefore, the chi-square approximation is applicable. For the same settings, the simulated Type I error probabilities  $P_1$  (for  $W_{10}$ ),  $P_2$  (for  $W_A^{10}$ ),  $P_3$  ( $W_{50}$ ) and  $P_4$  (for  $W_A^{50}$ ) are reported in Table 4. Under the null hypothesis  $H_0: \sigma_1^2 = \sigma_2^2 = \dots = \sigma_k^2$ , these are defined as

$$P_1 = \Pr \{W_{10} > F_{1-\alpha}(k-1, N-k) | H_0\}, P_2 = \Pr \{W_A^{10} > \chi_{1-\alpha}^2(\nu_{10}) | H_0\},$$

$$P_3 = \Pr \{W_{50} > F_{1-\alpha}(k-1, N-k) | H_0\}, P_4 = \Pr \{W_A^{50} > \chi_{1-\alpha}^2(\nu_{50}) | H_0\}.$$

It should be realized that  $P_2$  and  $P_4$  are equivalent to

$$P_2 = \Pr \{ W_{10} > c_{\alpha,10} \mid H_0 \} \text{ and } P_4 = \Pr \{ W_{50} > c_{\alpha,50} \mid H_0 \},$$

respectively.

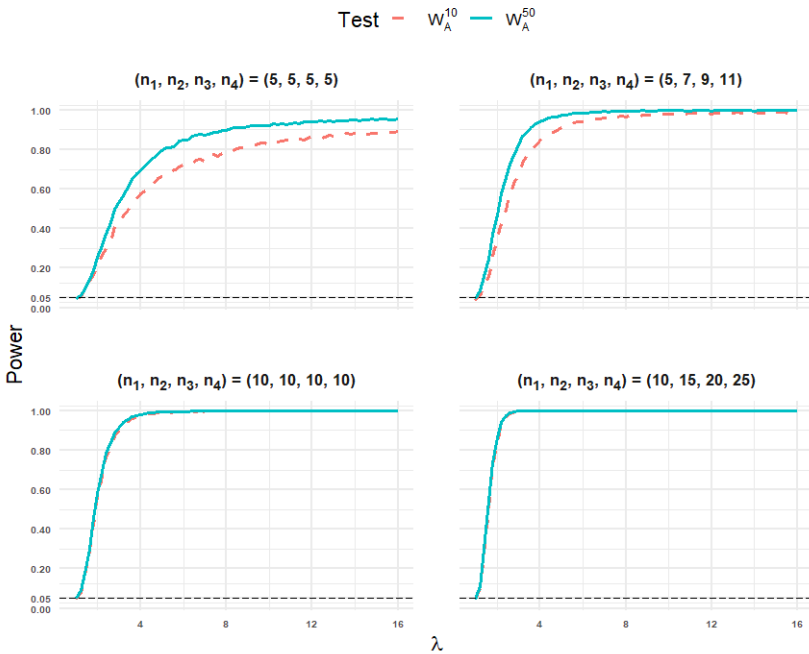
**Table 4.** Simulated Type I error probabilities  $P_1$  (for  $W_{10}$ ),  $P_2$  (for  $W_A^{10}$ ),  $P_3(W_{50})$  and  $P_4$  (for  $W_A^{50}$ ).

	$P_1$	$P_2$	$P_3$	$P_4$
Normal (0,1)				
(5,5,5,5)	0.089	0.048	0.003	0.049
(5,7,9,11)	0.077	0.049	0.011	0.048
(10,10,10,10)	0.059	0.050	0.027	0.049
(10,15,20,25)	0.062	0.048	0.035	0.049
Uniform (0,1)				
(5,5,5,5)	0.096	0.046	0.001	0.052
(5,7,9,11)	0.079	0.048	0.008	0.048
(10,10,10,10)	0.062	0.051	0.022	0.049
(10,15,20,25)	0.069	0.051	0.029	0.049
STS ( $r = 2, d = 0, \mu = 0, \sigma = 1$ )				
(5,5,5,5)	0.090	0.050	0.002	0.048
(5,7,9,11)	0.076	0.049	0.009	0.048
(10,10,10,10)	0.057	0.049	0.030	0.050
(10,15,20,25)	0.072	0.048	0.033	0.047
LTS ( $p = 3.5, \mu = 0, \sigma = 1$ )				
(5,5,5,5)	0.104	0.047	0.005	0.047
(5,7,9,11)	0.086	0.047	0.018	0.048
(10,10,10,10)	0.058	0.050	0.028	0.051
(10,15,20,25)	0.060	0.048	0.039	0.048
$\chi_5^2$				
(5,5,5,5)	0.153	0.045	0.008	0.047
(5,7,9,11)	0.139	0.047	0.025	0.051
(10,10,10,10)	0.088	0.049	0.037	0.045
(10,15,20,25)	0.102	0.048	0.045	0.049
Beta (10, 2)				
(5,5,5,5)	0.133	0.045	0.005	0.049
(5,7,9,11)	0.122	0.047	0.018	0.049
(10,10,10,10)	0.086	0.045	0.042	0.047
(10,15,20,25)	0.089	0.051	0.042	0.049

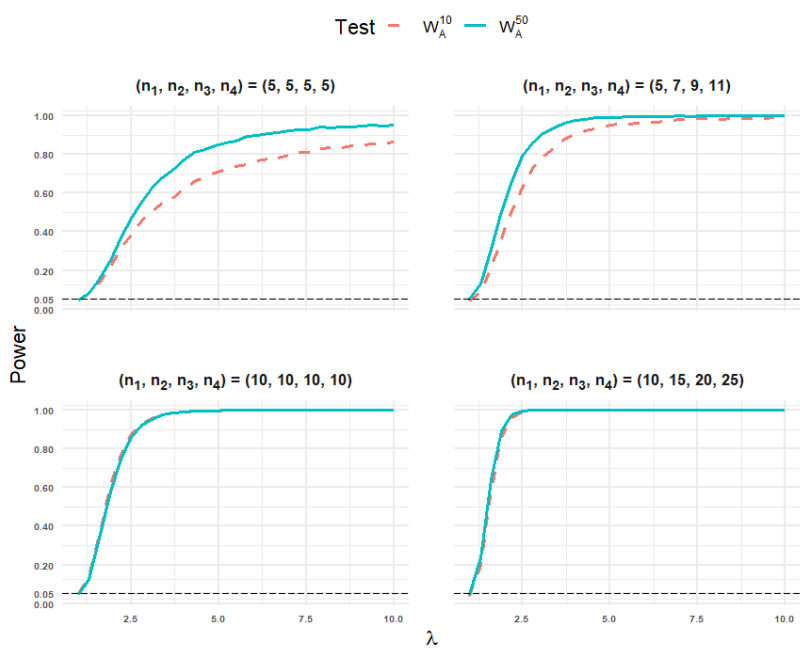
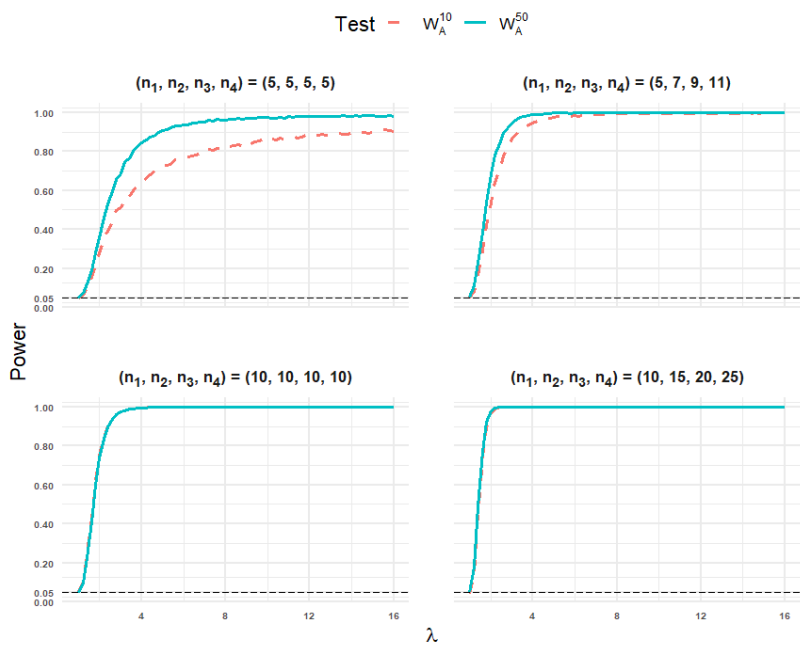
According to Table 4, the  $W_{10}$  test is liberal for both balanced and unbalanced sample sizes. On the other hand, the  $W_{50}$  test is conservative for all sample sizes except for the underlying distribution is  $\chi_5^2$  when the sample size is equal to (10,15,20,25) and  $Beta(10, 2)$  when the sample sizes are equal to (10,10,10,10) and (10,15,20,25). Realize that the distributions  $\chi_5^2$  and  $Beta(10, 2)$  are both

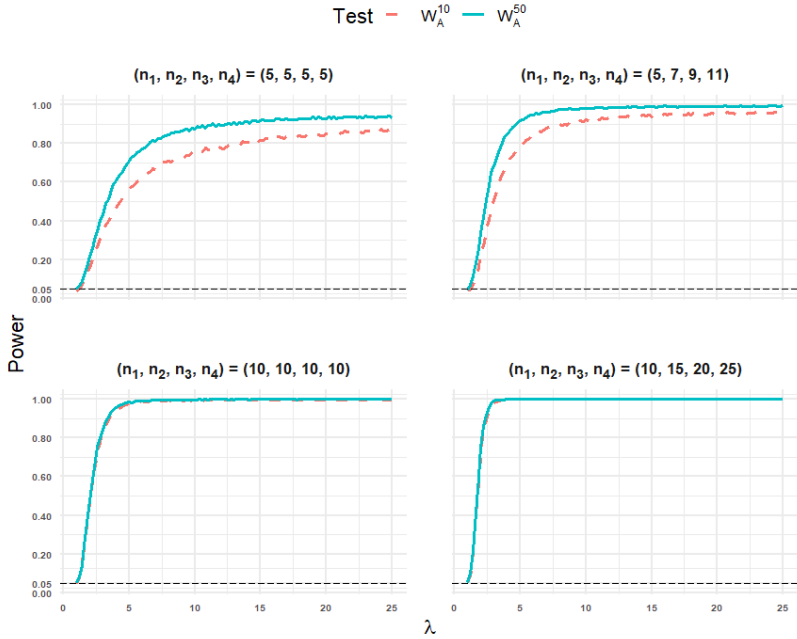
skewed. For  $W_A^{10}$  and  $W_A^{50}$ , the simulated Type I error rates are very close to the predetermined nominal level 0.050 regardless of the considered distributions and sample-size configurations.

Based on simulated Type I error rates, our attention is restricted to the  $W_A^{10}$  and  $W_A^{50}$  statistics to enable a meaningful and fair power comparison. Power values for  $W_A^{10}$  and  $W_A^{50}$  are presented in Figure 1 as a curves for different  $\lambda$  values, under the configurations of variance ratios  $\sigma_1^2 : \sigma_2^2 : \sigma_3^2 : \sigma_4^2 = 1 : \lambda : \lambda^2 : \lambda^3$  for both equal and unequal sample-size settings. It should be noted that when  $\lambda = 1$ , the configuration reduces to homoscedastic case, so the simulated power values are equal to the simulated Type I error rates.

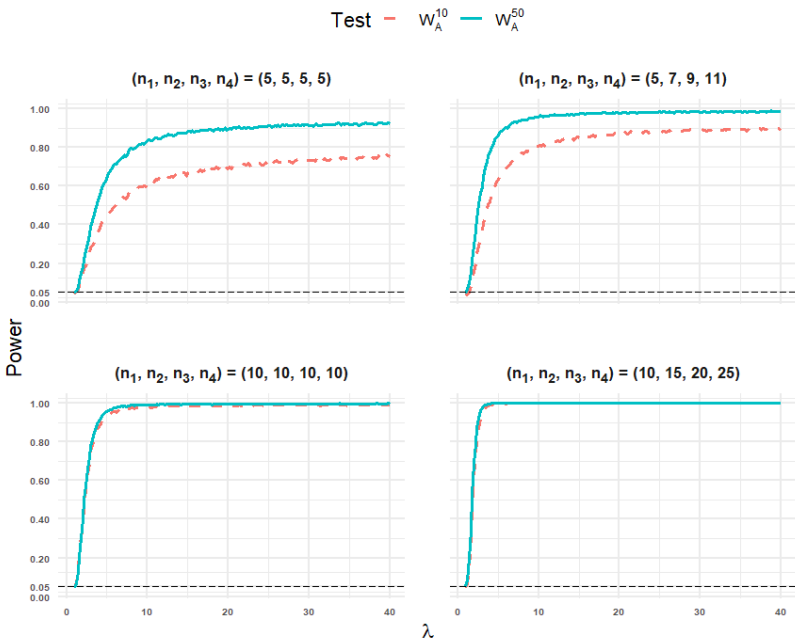


(a) Normal

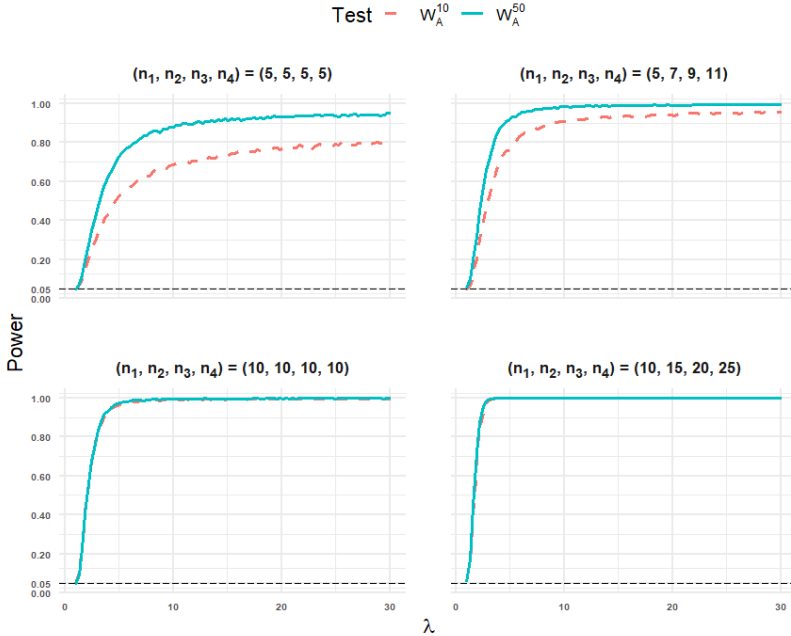




(d) LTS



(e) Chi-square



(f) Beta

**Figure 1.** Simulated power curves for  $W_A^{10}$  and  $W_A^{50}$  statistics under the configurations of variance ratios  $\sigma_1^2: \sigma_2^2: \sigma_3^2: \sigma_4^2 = 1: \lambda: \lambda^2: \lambda^3$  when the underlying distributions are Normal, Uniform, STS, LTS, Chi-Square and Beta.

The results in Figure 1 indicate that  $W_A^{50}$  test exhibits substantially greater power than  $W_A^{10}$  for small sample sizes, while the power advantage of  $W_A^{50}$  over  $W_A^{10}$  is particularly pronounced when the underlying distribution is skewed. For moderate sample sizes, two statistics show similar power performance regardless of whether sample sizes are equal or not. As expected, increasing  $\lambda$  (stronger heteroscedasticity) values lead to higher power values for both tests.

### 5 Concluding Remarks

In this study, we conducted a comparative assessment of Brown-Forsythe tests based on the 10% trimmed mean and the median, denoted  $W_{10}$  and  $W_{50}$ , respectively, for testing homogeneity of variances. These tests are widely used because they are robust to non-normality and straightforward to implement. Although they are often treated as approximately  $F$  distributed under the null hypothesis, the  $F$  reference distribution can yield size distortions from small to moderate samples under certain distributional settings. To better approximate the

null distribution of  $W_{10}$  and  $W_{50}$ , a three-moment chi-square approximation is used and moment-matched counterparts,  $W_A^{10}$  and  $W_A^{50}$  are defined. Accuracy of this approximation is investigated by Monte Carlo simulation for small and moderate sample sizes under symmetric and asymmetric distributions. Monte Carlo results show that  $W_{10}$  is liberal and  $W_{50}$  is conservative in general. On the other hand, the simulated Type I error rates of  $W_A^{10}$  and  $W_A^{50}$  are very close to the nominal level 0.050 across all distributional settings and designs. In addition,  $W_A^{50}$  exhibits higher power than  $W_A^{10}$  for small samples, with the advantage most pronounced under skewness. According to the simulation results,  $W_A^{50}$  is preferred for small-sample sizes while the use of either the  $W_A^{10}$  or the  $W_A^{50}$  statistic is recommended for moderate sample sizes. To the best of our knowledge, this is the first study that employs and evaluates a three-moment, chi-square approximation specifically for the Brown-Forsythe trimmed-mean and median tests. The methodology presented here can be extended to alternative distributional approximations in the context of variance-homogeneity in a future study.

## Appendix

*LTS Distribution:* The probability density function (pdf) of LTS distribution is

$$f(x) = \frac{1}{\sqrt{t}\beta(1/2, p-1/2)\sigma} \left(1 + \frac{(x-\mu)^2}{t\sigma^2}\right)^{-p}, \quad -\infty < x < \infty, p \geq 2, t = 2p - 3.$$

Here,  $\mu$ ,  $\sigma$  and  $p$  denote the location, scale and shape parameters, respectively. If random variable  $X$  is distributed as LTS, it is denoted by  $X \sim LTS(p, \mu, \sigma)$ . The mean and variance of  $X$  are  $E(X) = \mu$  and  $V(X) = \sigma^2$ , respectively. The kurtosis ( $\beta_2$ ) values of LTS distribution are given below for certain values of  $p$

$p =$	2.5	3.5	5	10	$\infty$
$\beta_2 =$	$\infty$	6	4.2	3.4	3

*STS Distribution:* The pdf of STS distribution is

$$f(x) = \frac{c}{\sqrt{2\pi}\sigma} \left(1 + \frac{\lambda}{2r} \left(\frac{x-\mu}{\sigma}\right)^2\right)^r \exp\left(-\frac{1}{2} \left(\frac{x-\mu}{\sigma}\right)^2\right), \quad -\infty < x < \infty,$$

where  $r$  is a constant,  $\lambda = r/(r - d)$ ,  $d < r$  and

$$C = 1/\sum_{j=0}^r \binom{r}{j} \left(\frac{\lambda}{2r}\right)^j ((2j)!/2^j(j)!).$$

Here,  $\mu$  and  $\sigma$  denote the location and scale parameters, respectively. If random variable  $X$  is distributed as STS, it is denoted by  $X \sim STS(r, d, \mu, \sigma)$ . The mean and variance of  $X$  are

$E(X) = \mu$  and  $V(X) = C \sum_{j=0}^r \binom{r}{j} \left(\frac{\lambda}{2r}\right)^j ((2(j+1))!/2^{j+1}(j+1)!) \sigma^2$ , respectively. The kurtosis ( $\beta_2$ ) values of STS distribution for certain values of  $d$  are given below when  $r = 2$  and 4

$d =$	-1	-0.5	0.0	0.5	1.0	1.5	2.5	3.5
$r = 2$								
	2.648	2.559	2.437	2.265	2.026	1.711	-	-
$r = 4$								
	2.541	2.464	2.370	2.255	2.118	1.957	1.591	1.297

Here, the dashed entries are used for  $d > r$  since the kurtosis values are defined when  $d < r$  and it is clearly seen that the kurtosis values are less than 3.

## References

- Bartlett, M. S. (1937). Properties of sufficiency and statistical tests. *Proceedings of the royal society of london. series a-mathematical and physical sciences*, 160(901), 268-282.
- Brown, M. B., & Forsythe, A. B. (1974). Robust tests for the equality of variances. *Journal of the American statistical association*, 69(346), 364-367.
- Cahoy, D. O. (2010). A bootstrap test for equality of variances. *Computational statistics & data analysis*, 54(10), 2306-2316.
- Cochran, W. G. (1937). Problems arising in the analysis of a series of similar experiments. *Supplement to the Journal of the Royal Statistical Society*, 4(1), 102-118.
- Conover, W. J., Johnson, M. E., & Johnson, M. M. (1981). A comparative study of tests for homogeneity of variances, with applications to the outer continental shelf bidding data. *Technometrics*, 23(4), 351-361.
- Ederington, L. H., & Lee, J. H. (1993). How markets process information: News releases and volatility. *The Journal of Finance*, 48(4), 1161-1191.
- Elamir, E. A. (2023). Assessing homoscedasticity graphically: levene-brown-forsythe approaches. *Revstat-Statistical Journal*, 21(3), 389-404.
- Esi, B., & Baykal, P. D. (2020). Investigation of tensile strength and elongation properties of chenille upholstery fabrics including recycling polyester yarns. *Journal of Engineered Fibers and Fabrics*, 15, 1558925020916040.
- Esmailzadeh, N. (2019). A comparison of five bootstrap and non-bootstrap levene-type tests of homogeneity of variances. *Iranian Journal of Science and Technology, Transactions A: Science*, 43(3), 979-989.
- Gastwirth, J. L., Gel, Y. R., & Miao, W. (2009). The impact of Levene's test of equality of variances on statistical theory and practice. *Statistical Science*, 24(3), 343-360.
- Güven, G. (2023). Testing equality of means in one-way ANOVA using three and four moment approximations. *Communications Faculty of Sciences University of Ankara Series A1 Mathematics and Statistics*, 72(3), 587-605.
- Jayalath, K. P., Ng, H. K. T., Manage, A. B., & Riggs, K. E. (2017). Improved tests for homogeneity of variances. *Communications in Statistics-Simulation and Computation*, 46(9), 7423-7446.
- Layard, M. W. (1973). Robust large-sample tests for homogeneity of variances. *Journal of the American Statistical Association*, 68(341), 195-198.

- Levene, H. (1960) Robust Tests for Equality of Variances. In: Olkin, I., Ed., Contributions to Probability and Statistics, Stanford University Press, Palo Alto, 278-292.
- Li, D., Lin, S. K., & Li, C. (1997). The impact of settlement time on the volatility of stock markets. *Applied Financial Economics*, 7(6), 689-694.
- Li, X., Qiu, W., Morrow, J., DeMeo, D. L., Weiss, S. T., Fu, Y., & Wang, X. (2015). A comparative study of tests for homogeneity of variances with application to DNA methylation data. *PloS one*, 10(12), e0145295.
- Lim, T. S., & Loh, W. Y. (1996). A comparison of tests of equality of variances. *Computational Statistics & Data Analysis*, 22(3), 287-301.
- Pearson, E. S. (1959). Note on an approximation to the distribution of non-central  $\chi^2$ . *Biometrika*, 46(3/4), 364.
- Sarkar, S., Kim, C., & Basu, A. (1999). Tests for homogeneity of variances using robust weighted likelihood estimates. *Biometrical Journal: Journal of Mathematical Methods in Biosciences*, 41(7), 857-871.
- Sharma, D., & Kibria, B. G. (2013). On some test statistics for testing homogeneity of variances: a comparative study. *Journal of Statistical Computation and Simulation*, 83(10), 1944-1963.
- Sharma, S. C. (1991). A new jackknife test for homogeneity of variances. *Communications in Statistics-Simulation and Computation*, 20(2-3), 479-495.
- Stephens, M. A. (1964). The Distribution of the Goodness-of-fit Statistic,  $U^2_N$ . II. *Biometrika*, 51(3/4), 393-397.
- Sürücü, B., & Sazak, H. S. (2009). Monitoring reliability for a three-parameter Weibull distribution. *Reliability Engineering & System Safety*, 94(2), 503-508.
- Tiku, M. L. (1965). Chi-Square Approximations for the Distributions of Goodness-Of-Fit Statistics  $U^2_n$  and  $W^2_n$ . *Biometrika*, 52(3/4), 630-633.
- Tiku, M. L., & Kumra, S. (1985). Expected values and variances and covariances of order statistics for a family of symmetrical distributions (Student's t). In W. J. Kennedy, R. E. Odeh, & J. M. Davenport (Eds.), *Selected tables in mathematical statistics* (Vol. 8, pp. 141-270). American Mathematical Society.
- Tiku, M. L., & Wong, W. K. (1998). Testing for a unit root in an AR (1) model using three and four moment approximations: symmetric distributions. *Communications in Statistics-Simulation and Computation*, 27(1), 185-198.

- Tiku, M. L., & Vaughan, D. C. (1999). A family of short-tailed symmetric distributions. Unpublished Tech. Rep. McMaster University, Canada.
- Zhou, Y., Zhu, Y., & Wong, W. K. (2023). Statistical tests for homogeneity of variance for clinical trials and recommendations. *Contemporary clinical trials communications*, 33, 101119.

## Chapter 2

---

# Photodetection and Solar Energy Harvesting Using Schottky Junctions

İlhan CANDAN<sup>1</sup>, Sezai ASUBAY<sup>2</sup>

### Abstract

Schottky junctions, formed at the interface between a metal and a semiconductor, play a critical role in modern optoelectronics due to their unique ability to facilitate ultrafast charge separation without requiring p–n junctions. This chapter explores the physical principles, material systems, and device architectures underpinning the application of Schottky junctions in photodetection and solar energy harvesting. By exploiting the built-in electric field at the metal–semiconductor interface, Schottky devices enable efficient carrier extraction, making them highly suitable for broadband photodetectors, infrared sensors, and low-cost photovoltaic systems. The chapter begins by discussing the fundamentals of Schottky barrier formation, Fermi-level pinning, and charge transport mechanisms, including thermionic emission and tunneling. It then reviews a wide range of materials used in Schottky-based devices, including traditional semiconductors like silicon, compound semiconductors such as GaAs and InGaN, and emerging materials like two-dimensional semiconductors and metal oxides. A key focus is on Schottky solar cells, which offer simplified architectures and potential cost advantages over conventional p–n junction solar cells. We also explore hot-carrier injection in plasmonic metal–semiconductor interfaces, an approach that leverages light–matter interaction at the nanoscale to surpass traditional efficiency limits. Finally, the chapter outlines current challenges such as barrier height optimization, interface stability, and contact engineering, along with recent strategies to address them. Through a combination of theoretical insights and practical examples, this chapter provides a comprehensive understanding of how photodetection technologies. -generation light-harvesting and Schottky junctions are being harnessed for next

---

<sup>1</sup> Asist. Prof. Dr. Dicle University, Science Faculty, Dept. of Physics, 21280 Diyarbakır Turkey, Orcid no: 0000-0001-9489-5324

<sup>2</sup> Prof. Dr. Dicle University, Science Faculty, Dept. of Physics, 21280 Diyarbakır Turkey<sup>7</sup> Orcid no: 0000-0003-2171-8479

## 1. Introduction

The continuous demand for efficient energy conversion and advanced optoelectronic devices has driven significant research into novel materials and architectures for photodetection and solar energy harvesting [1, 2]. Among various approaches, Schottky junctions—formed at the metal–semiconductor interface—have emerged as a promising platform due to their unique electronic and optical properties [3]. Unlike conventional p–n junctions, Schottky contacts rely on the rectifying barrier created by the work function difference between a metal and a semiconductor, enabling ultrafast carrier transport, low fabrication complexity, and compatibility with diverse material systems [4, 5].

In the context of photodetection, Schottky junctions offer several advantages [6, 7]. The built-in electric field at the interface facilitates rapid separation of photogenerated carriers, yielding fast response times and broad spectral sensitivity. By carefully engineering the choice of metal, semiconductor, and interface quality, Schottky-based photodetectors can achieve high responsivity and detectivity across ultraviolet, visible, and infrared regimes. Additionally, their relatively simple structure allows integration into flexible and transparent platforms, which is attractive for next-generation wearable and biomedical sensors.

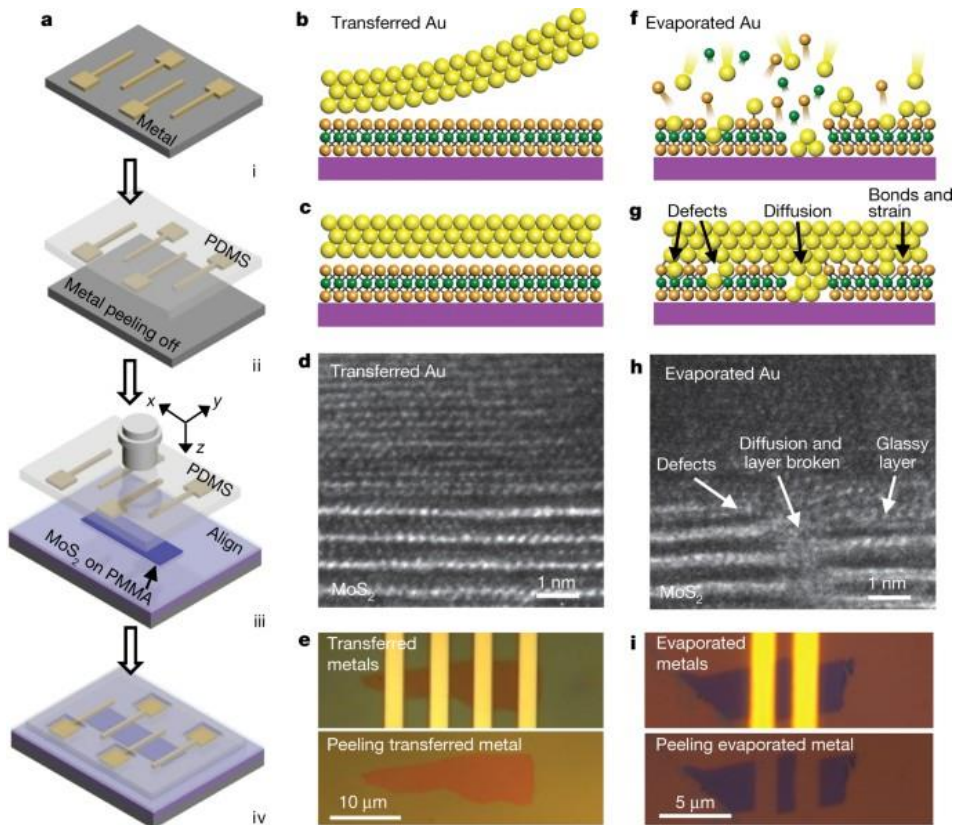
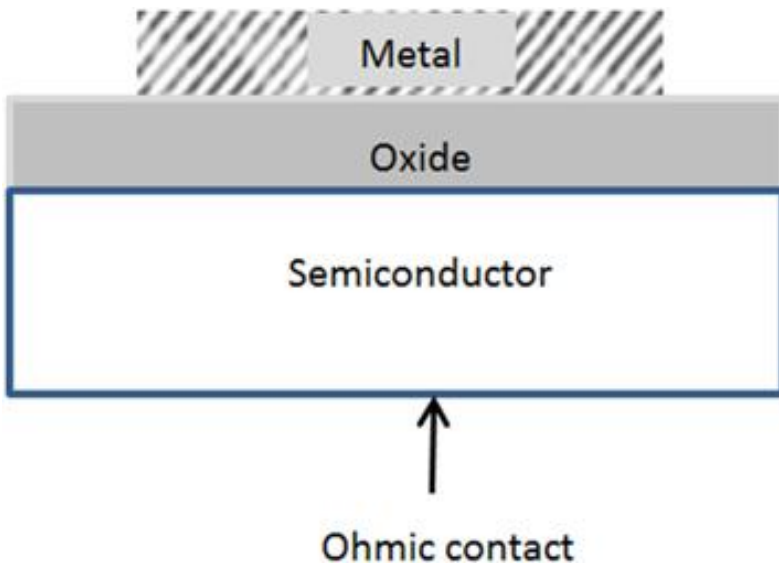


Figure 1. (a) Schematic illustration of the van der Waals (vdW) integration process for metal–semiconductor junctions: (i) deposition of a metal film onto a sacrificial substrate; (ii) delamination of the metal layer; (iii) alignment with the target semiconductor; and (iv) lamination of the contact followed by probe window opening. (b–d) Cross-sectional schematics and transmission electron microscopy (TEM) images of transferred Au electrodes on MoS<sub>2</sub>, showing atomically sharp and contamination-free metal–semiconductor interfaces. (e) Optical micrographs of a MoS<sub>2</sub> device with transferred electrodes (top) and after mechanical release of the electrodes (bottom). The MoS<sub>2</sub> layer remains intact following integration and separation of the Au thin film, confirming that the transferred interface is dominated by vdW interactions without direct chemical bonding. (f–h) In contrast, cross-sectional schematics and TEM images of conventionally electron-beam-deposited Au electrodes on MoS<sub>2</sub> reveal significant interfacial damage. High-energy Au atoms and clusters bombard the MoS<sub>2</sub> surface, leading to defect generation, interdiffusion, chemical bonding, and the formation of a disordered glassy layer. (i) Optical images further demonstrate

this difference: when deposited electrodes are mechanically removed, the underlying MoS<sub>2</sub> surface is severely damaged, indicating strong chemical bonding and direct metal–semiconductor interactions in deposited junctions [3].

For solar energy harvesting, Schottky junction solar cells provide an alternative to traditional silicon-based devices [8, 9]. Although they typically exhibit lower efficiency compared to optimized p–n junction cells, they offer unique benefits, such as low-cost fabrication, tunable spectral absorption, and the potential to exploit hot-carrier effects. Recent progress in nanostructuring, plasmonic enhancement, and two-dimensional (2D) semiconductors has further expanded the scope of Schottky junction photovoltaics. By combining nanoscale engineering with advanced materials, researchers are addressing fundamental challenges such as barrier height control, recombination losses, and light absorption enhancement.



**Figure 2.** MOS structure’s schematic diagram [10].

This chapter provides an overview of the fundamental principles of Schottky junctions, their role in photodetection and solar energy harvesting, and recent advancements that highlight their potential as building blocks for future optoelectronic technologies.

## 2. Fundamentals of Schottky Junctions

### 2.1 Formation and Energy Band Structure

A Schottky junction is formed when a metal with an appropriate work function is brought into contact with a semiconductor. At thermal equilibrium, the difference in Fermi levels leads to the formation of a depletion region in the semiconductor and a built-in potential at the interface [11, 12].

For an n-type semiconductor, if the metal work function  $\phi_m$  is greater than the semiconductor electron affinity  $\chi$ , a barrier is formed for electron flow from the semiconductor to the metal, known as the Schottky barrier height (SBH). The ideal SBH is given by:

$$\phi_{Bn} = \phi_m - \chi \quad (1)$$

In practice, however, Fermi level pinning and interface states can modify the effective barrier height.

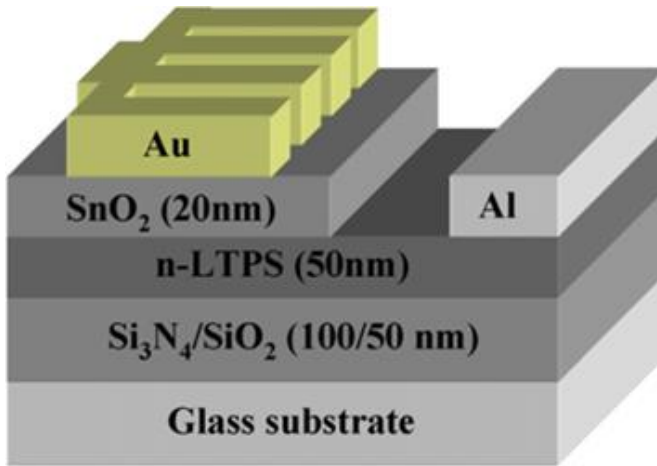


**Figure 3.** Au/SnO<sub>2</sub>/n-LTPS MOS Schottky diode's schematic cross-section [10, 13].

### 2.2 Current Transport Mechanisms

Current through a Schottky junction under forward bias occurs primarily via thermionic emission, where electrons overcome the potential barrier [14, 15]. The current density  $J$  is described by the Richardson equation:

$$J = A * T^2 \exp\left(-\frac{q\phi_{Bn}}{kT}\right) \left[\exp\left(\frac{qV}{nkT}\right) - 1\right] \quad (2)$$

Where:

- $A^*$  is the Richardson constant,
- $T$  is temperature,
- $\phi_{Bn}$  is the barrier height,
- $n$  is the ideality factor,
- $V$  is applied voltage.

### 3. Schottky Junctions in Photodetectors

#### 3.1 Working Principle

Photodetectors based on Schottky junctions operate by converting incident photons into electrical signals. When light with energy  $h\nu > E_g$  strikes the semiconductor side of the junction, electron-hole pairs are generated [6]. The built-in electric field at the Schottky barrier separates the charge carriers, allowing for a photocurrent to be measured.

Unlike photoconductive detectors, Schottky photodiodes are typically faster due to the short transit time across the depletion region and low capacitance.

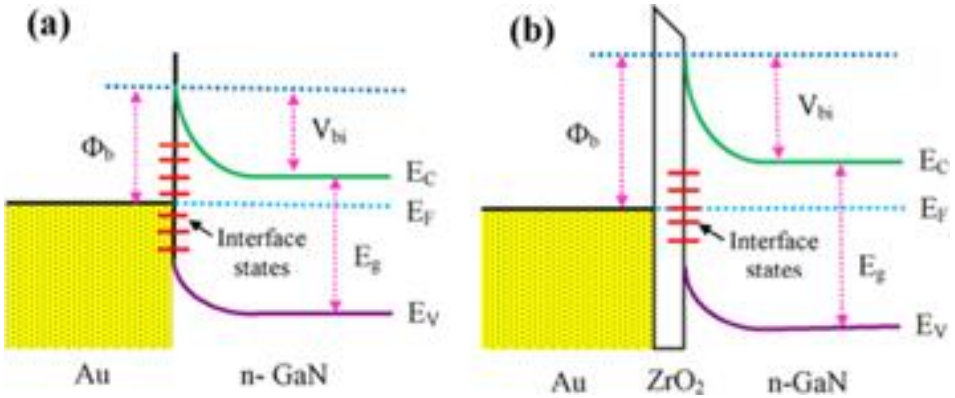


Figure 4. (a) Current–voltage (I–V) characteristics and (b) variation of the surface state density (NSS) as a function of EC–ESS for Au/n-GaN and Au/ZrO<sub>2</sub>/n-GaN Schottky junctions. The inset shows the schematic structure of the Au/ZrO<sub>2</sub>/n-GaN diode [16].

### ***3.2 Key Performance Parameters***

- Responsivity (R): The output current per unit incident optical power, typically in A/W.
- Quantum Efficiency (QE): The ratio of the number of charge carriers collected to the number of incident photons.
- Response Time: Time taken by the device to respond to an optical signal.
- *\*Detectivity (D)\*\**: A measure of the signal-to-noise ratio, often used for low-light applications.

The performance of Schottky photodetectors is commonly characterized using several key parameters that determine their suitability for various photodetection applications. Responsivity (R) represents the output current generated per unit of incident optical power and is typically expressed in amperes per watt (A/W). It reflects the device's ability to convert incoming light into an electrical signal. Quantum efficiency (QE), on the other hand, defines the ratio of the number of charge carriers collected to the number of incident photons, providing a measure of how efficiently the device utilizes incoming photons for charge generation. Another important characteristic is the response time, which indicates how quickly the photodetector reacts to variations in the optical signal—an essential factor for high-speed communication and imaging applications. Lastly, detectivity (D) serves as a measure of the signal-to-noise ratio, describing the detector's capability to sense weak optical signals, particularly in low-light environments. High detectivity is especially desirable for applications requiring sensitive light detection, such as night vision, astronomy, and remote sensing.

### ***3.3 Material Systems for Schottky Photodetectors***

Several materials have been employed to enhance the performance of Schottky photodetectors:

- Silicon (Si): Widely used due to its mature fabrication technology, suitable for visible to near-infrared detection.
- Gallium Arsenide (GaAs): Offers higher electron mobility and absorption efficiency.
- Two-Dimensional Materials (e.g., MoS<sub>2</sub>, graphene): Enable ultrafast and broadband photodetection with sub-nanometer thicknesses.

- Plasmonic Metals (Au, Ag): Used to enhance light absorption via surface plasmon resonance.

To improve the efficiency and functionality of Schottky photodetectors, a variety of materials have been explored and integrated into device architectures. Silicon (Si) remains the most widely used material owing to its well-established fabrication technology and compatibility with existing semiconductor processing, making it particularly suitable for photodetection across the visible to near-infrared spectral range. Gallium arsenide (GaAs) is another prominent material that offers superior electron mobility and higher optical absorption efficiency compared to silicon, enabling faster response times and enhanced sensitivity. In recent years, two-dimensional (2D) materials such as molybdenum disulfide (MoS<sub>2</sub>) and graphene have attracted significant attention due to their exceptional electronic and optical properties, ultrafast carrier dynamics, and atomic-scale thickness, which facilitate broadband and ultrafast photodetection. Additionally, plasmonic metals such as gold (Au) and silver (Ag) have been incorporated to enhance light absorption through surface plasmon resonance effects, thereby boosting the overall photoresponse of Schottky-based detectors. The strategic combination of these materials continues to drive innovation in high-performance, miniaturized, and energy-efficient photodetection technologies.

### ***3.4 Applications***

Schottky photodetectors have found widespread applications across a range of advanced optical and electronic systems due to their fast response times, high sensitivity, and compatibility with various semiconductor materials. They are extensively employed in optical communication systems, where rapid detection of optical signals is essential for high-speed data transmission. In addition, Schottky photodetectors are well-suited for ultraviolet (UV) and X-ray detection owing to their ability to operate efficiently at short wavelengths and their low dark current characteristics. These devices are also utilized in imaging sensors, where their excellent temporal resolution enhances image quality and enables high-speed image capture. Furthermore, Schottky photodetectors play an important role in light detection and ranging (LIDAR) as well as time-of-flight (ToF) systems, contributing to precise distance measurement and three-

dimensional imaging in applications such as autonomous vehicles and remote sensing.

## **4. Schottky Junctions in Solar Energy Harvesting**

### ***4.1 Operating Principle of Schottky Solar Cells***

Schottky solar cells leverage the same metal-semiconductor junction to separate photo-generated carriers [17]. However, compared to p–n junction solar cells, Schottky devices often suffer from lower open-circuit voltage due to high recombination rates and limited built-in potential.

Nevertheless, their simplified structure, low-temperature fabrication, and tunability of barrier height via material selection make them attractive for niche photovoltaic applications [18].

### ***4.2 Device Architectures***

Typical Schottky solar cells consist of:

- Front contact metal (forming the Schottky barrier)
- Semiconductor absorber (e.g., Si, GaAs, perovskites)
- Back contact (ohmic or Schottky, depending on design)

Advanced architectures may include:

- Core–shell nanostructures
- Transparent conducting oxides (TCOs) as front electrodes
- Plasmonic nanoparticles for light trapping and absorption enhancement

### ***4.3 Material Choices***

Metals: Au, Ag, Al, and Pt are commonly used, chosen based on their work function and optical properties.

Semiconductors:

- Si and GaAs: Conventional, well-studied choices.
- ZnO and TiO<sub>2</sub>: Used in ultraviolet and dye-sensitized solar cells.
- Organic semiconductors: Enable flexible, lightweight solar devices.
- 2D materials: Offer unique opportunities for tunable bandgaps and ultra-thin devices.

#### ***4.4 Performance Challenges and Strategies***

Challenges in Schottky solar cells include:

- Low open-circuit voltage ( $V_{oc}$ ) due to small built-in potential.
- Interface recombination at the metal-semiconductor contact.
- Fermi level pinning limiting tunability of barrier height.

To overcome these, several strategies are used:

- Insertion of interfacial layers (e.g., oxide barriers) to passivate defects.
- Use of high work function metals to increase barrier height.
- Nanostructuring to increase light absorption and carrier collection.

### **5. Emerging Trends and Research Directions**

#### ***5.1 Plasmonic Enhancement***

Integrating plasmonic nanoparticles (e.g., Au nanospheres) with Schottky devices can significantly enhance light absorption due to local field enhancement and hot-electron injection mechanisms. These effects are especially beneficial in sub-bandgap photon utilization and broadband absorption [19].

#### ***5.2 Schottky Junctions with 2D Materials***

Atomically thin materials like graphene and transition metal dichalcogenides (TMDs) have emerged as promising candidates for Schottky-based devices [20]. These materials offer:

- Tunable electronic and optical properties
- High carrier mobility
- Minimal bulk recombination

Graphene/semiconductor Schottky solar cells have demonstrated enhanced transparency, flexibility, and mechanical robustness.

#### ***5.3 Flexible and Transparent Devices***

Schottky junctions are particularly suited for flexible and transparent electronics [21, 22]. Using metal nanowires, conductive polymers, or ultrathin films, researchers are developing conformable photodetectors and solar cells for wearable and portable systems.

### ***5.4 Integration with CMOS and Photonic Platforms***

The compatibility of Schottky diodes with standard CMOS processes enables their integration into existing electronic and photonic circuits [23]. Applications include on-chip photodetectors, optical interconnects, and monolithic integration of photovoltaic cells.

### ***Future Perspectives***

The future of Schottky junction-based devices lies in the convergence of advanced materials and innovative device architectures. One promising direction is the integration of two-dimensional (2D) materials such as graphene, MoS<sub>2</sub>, and other transition metal dichalcogenides with metals to form tunable Schottky contacts. Their atomically thin nature enables precise control over barrier height, reduced recombination losses, and flexible, transparent optoelectronic platforms. Similarly, perovskite-metal hybrid junctions have gained attention for solar energy harvesting, where the unique optoelectronic properties of perovskites combined with Schottky interfaces can potentially yield high-efficiency, low-cost devices.

In photodetection, future research is expected to focus on multifunctional Schottky detectors that combine high-speed response with broadband sensitivity, while exploiting plasmonic and hot-carrier effects to extend detection into the mid-infrared region. For solar cells, innovations in nanophotonic light management and quantum-engineered structures may allow Schottky junctions to surpass some of their traditional efficiency limits.

Ultimately, the continued synergy between materials discovery, nanoscale fabrication, and theoretical modeling will determine how far Schottky junction technologies can advance, with the potential to redefine next-generation optoelectronics and sustainable energy solutions.

## **6. Conclusion**

Schottky junctions, based on the rectifying interface between metals and semiconductors, have demonstrated considerable promise in advancing both photodetection and solar energy harvesting technologies. Their fundamental advantage lies in the intrinsic electric field at the metal-semiconductor interface, which enables efficient carrier separation, rapid response times, and broad spectral tunability without requiring complex doping processes. This makes them

attractive for applications ranging from ultraviolet and infrared photodetectors to thin-film and nanostructured photovoltaic devices.

In photodetection, Schottky junction devices benefit from their inherently fast carrier dynamics, enabling high-speed operation crucial for optical communication, imaging, and sensing. By leveraging plasmonic effects, interface engineering, and novel material platforms such as two-dimensional semiconductors, their performance has been extended toward enhanced sensitivity, lower noise levels, and adaptability to flexible and transparent substrates.

For solar energy harvesting, Schottky junctions offer an alternative to conventional p–n junction solar cells, particularly in applications where cost, weight, and ease of fabrication are critical. While their conversion efficiencies are currently lower than those of mature silicon technologies, significant progress has been made in overcoming limitations through barrier height optimization, nanostructuring for enhanced light trapping, and the integration of advanced materials. These strategies have opened pathways toward exploiting hot-carrier phenomena and plasmonic enhancement, potentially pushing Schottky-based solar devices into new realms of efficiency and functionality.

Looking forward, the synergy between nanotechnology, materials innovation, and device engineering will be essential in realizing the full potential of Schottky junctions. Continued research efforts aimed at addressing stability, scalability, and interfacial control will determine their broader adoption in commercial applications. Ultimately, Schottky junctions stand as a versatile platform, bridging fundamental physics with practical optoelectronic solutions, and offering exciting prospects for next-generation photodetection and renewable energy technologies.

## References

- [1] L. Peng, L. Hu, and X. Fang, "Energy harvesting for nanostructured self-powered photodetectors," *Advanced Functional Materials*, vol. 24, no. 18, pp. 2591-2610, 2014.
- [2] N. Ilyas *et al.*, "Nanostructured materials and architectures for advanced optoelectronic synaptic devices," *Advanced Functional Materials*, vol. 32, no. 15, p. 2110976, 2022.
- [3] Y. Liu *et al.*, "Approaching the Schottky–Mott limit in van der Waals metal–semiconductor junctions," *Nature*, vol. 557, no. 7707, pp. 696-700, 2018.
- [4] Y. Xu *et al.*, "Contacts between two-and three-dimensional materials: Ohmic, Schottky, and p–n heterojunctions," *ACS nano*, vol. 10, no. 5, pp. 4895-4919, 2016.
- [5] L. Lv *et al.*, "Design and tailoring of two-dimensional Schottky, PN and tunnelling junctions for electronics and optoelectronics," *Nanoscale*, vol. 13, no. 14, pp. 6713-6751, 2021.
- [6] J.-Y. Wu, H.-Y. Jiang, Z.-Y. Wen, and C.-R. Wang, "Fundamental and photodetector application of van der Waals Schottky junctions," *Advanced Devices & Instrumentation*, vol. 4, p. 0022, 2023.
- [7] B. Ezhilmaran *et al.*, "Recent developments in the photodetector applications of Schottky diodes based on 2D materials," *Journal of Materials Chemistry C*, vol. 9, no. 19, pp. 6122-6150, 2021.
- [8] E. Goulielmakis *et al.*, "Real-time observation of valence electron motion," *Nature*, vol. 466, no. 7307, pp. 739-743, 2010.
- [9] R. V. Chavali, S. De Wolf, and M. A. Alam, "Device physics underlying silicon heterojunction and passivating-contact solar cells: A topical review," *Progress in Photovoltaics: Research and Applications*, vol. 26, no. 4, pp. 241-260, 2018.
- [10] N. A. Al-Ahmadi, "Metal oxide semiconductor-based Schottky diodes: a review of recent advances," *Materials Research Express*, vol. 7, no. 3, p. 032001, 2020.
- [11] İ. Taşçıoğlu, Ş. Altındal, İ. Polat, and E. Bacaksız, "The effect of metal work function on the barrier height of metal/CdS/SnO<sub>2</sub>/In–Ga structures," *Current Applied Physics*, vol. 13, no. 7, pp. 1306-1310, 2013.

- [12] J. Meng, C. Lee, and Z. Li, "Adjustment methods of Schottky barrier height in one-and two-dimensional semiconductor devices," *Science Bulletin*, vol. 69, no. 9, pp. 1342-1352, 2024.
- [13] F.-R. Juang, Y.-K. Fang, Y.-T. Chiang, T.-H. Chou, C.-I. Lin, and C.-W. Lin, "The low temperature polysilicon (LTPS) thin film MOS Schottky diode on glass substrate for low cost and high performance CO sensing applications," *Sensors and Actuators B: Chemical*, vol. 156, no. 1, pp. 338-342, 2011.
- [14] H. Kim, "A review on reverse-bias leakage current transport mechanisms in metal/GaN Schottky diodes," *Transactions on Electrical and Electronic Materials*, vol. 25, no. 2, pp. 141-152, 2024.
- [15] S. Mukhopadhyay, L. A. Lyle, H. Pal, K. K. Das, L. M. Porter, and B. Sarkar, "Evidence of thermionic emission in forward biased  $\beta$ -Ga<sub>2</sub>O<sub>3</sub> Schottky diodes at Boltzmann doping limit," *Journal of Applied Physics*, vol. 131, no. 2, 2022.
- [16] V. R. Reddy and C. V. Prasad, "Surface chemical states, electrical and carrier transport properties of Au/ZrO<sub>2</sub>/n-GaN MIS junction with a high-k ZrO<sub>2</sub> as an insulating layer," *Materials Science and Engineering: B*, vol. 231, pp. 74-80, 2018.
- [17] P. Kumari, N. Bahadur, L. Kong, L. A. O'Dell, A. Merenda, and L. F. Dumée, "Engineering Schottky-like and heterojunction materials for enhanced photocatalysis performance—a review," *Materials Advances*, vol. 3, no. 5, pp. 2309-2323, 2022.
- [18] A. Polman, M. Knight, E. C. Garnett, B. Ehrler, and W. C. Sinke, "Photovoltaic materials: Present efficiencies and future challenges," *Science*, vol. 352, no. 6283, p. aad4424, 2016.
- [19] A. Zada *et al.*, "Surface plasmonic-assisted photocatalysis and optoelectronic devices with noble metal nanocrystals: design, synthesis, and applications," *Advanced Functional Materials*, vol. 30, no. 7, p. 1906744, 2020.
- [20] B. Das and R. Ghosh, "Emerging 2D Materials for Gas Sensor," in *Emerging Materials for Energy and Sensing Applications*: CRC Press, 2025, pp. 139-154.
- [21] J. Wager, "Transparent electronics: Schottky barrier and heterojunction considerations," *Thin Solid Films*, vol. 516, no. 8, pp. 1755-1764, 2008.

- [22] S. Ying *et al.*, "Device based on polymer Schottky junctions and their applications: a review," *IEEE Access*, vol. 8, pp. 189646-189660, 2020.
- [23] N. Izhaky *et al.*, "Development of CMOS-compatible integrated silicon photonics devices," *IEEE Journal of Selected Topics in Quantum Electronics*, vol. 12, no. 6, pp. 1688-1698, 2007.

# Performance Evaluation of Numerical Root Finding Methods Using Fibonacci and Golden Ratio Algorithms

Bayram KÖSE<sup>1</sup>, Bahar DEMİRTÜRK<sup>2</sup>, Şükran KONCA<sup>3</sup>

### Abstract

Root finding techniques are essential in numerical methods for solving complex engineering equations when analytical methods are insufficient. These techniques efficiently locate the zeros (roots) of a function, minimizing computational effort. They are also crucial in optimization problems to find the minimum value of a function. For example, root finding problems may be encountered, such as the intersection points of gears with different numbers of teeth, the moments when the current in an electric circuit is zero, the moments when the electric field along the line connecting two interacting charges is zero, or the calculation of function roots when calculating the eigenvalues of a system. The root finding method is also used in optimization problems. In optimization algorithm, root search is a method used to find the minimum value of a function. In this method, we try to find the point where the function is closest to zero by calculating the values of the function at points within a range. This point gives the minimum of the function. If the function has more than one minima, the root search method can find only one of them. This is one of the disadvantages of the root search method. Also, it may require a lot of processing to calculate the values of the function. Therefore, more efficient and faster optimization algorithms continue to be developed. Algebraic properties are vital in designing efficient algorithms, and the choice of algorithm depends on the function's characteristics.

When we look at recent studies; Gemechu and Thota (Gemechu and Thota, 2020) developed new iteration algorithms for finding the root of a given nonlinear equation using nonlinear Taylor polynomial interpolation and an error correction term modified by the concept of fixed point. Thota (Thota, 2019) developed a new root-finding algorithm using exponential series. Sabharwa (Sabharwa, 2019)

---

<sup>1</sup> İzmir Bakırçay University, Faculty of Engineering and Architecture, Department of Electrical and Electronics Engineering, 35660 Menemen, İzmir, Türkiye. \* bayram.kose@bakircay.edu.tr

<sup>2</sup> İzmir Bakırçay University, Faculty of Engineering and Architecture, Department of Fundamental Sciences, 35660 Menemen, İzmir, Türkiye. bahar.demirturk@bakircay.edu.tr,

<sup>3</sup> İzmir Bakırçay University, Faculty of Engineering and Architecture, Department of Fundamental Sciences, 35660 Menemen, İzmir, Türkiye. sukran.konca@bakircay.edu.tr

designed and implemented a new algorithm that is a dynamic mixture of halving and regula falsi algorithms. Semenov (Semenov, 2015) proposed a method for computing all roots of systems of nonlinear algebraic equations in a multidimensional interval based on the Krawczyk operator. Vatansever and Hatun (Vatansever and Hatun, 2015) developed a graphical interface program based on Newton methods.

This study analyzes the performance of the Fibonacci search algorithm and the golden ratio search algorithm in finding the roots of selected polynomial, trigonometric, and logarithmic test functions. The results from these methods are compared by calculating the absolute error, average absolute error, and average approximation errors to determine the most efficient approach with the least error. Using Matlab, we obtained these error metrics by comparing the number of iterations required to find the roots for each algorithm, the proximity of the roots found by each algorithm, and the results against the actual root values. The findings were evaluated to provide insights and recommendations on which algorithm is preferable in different scenarios based on numerical stability. Finally, we assessed the results and offered suggestions on the optimal algorithm choice for various situations considering numerical stability.

**Keywords.** Root-finding algorithms, Optimization algorithms, Golden ratio search algorithm, Fibonacci search algorithm.

## 1. INTRODUCTION

Fibonacci numbers, which also form the basis of mathematical concepts such as the Golden Ratio and Pascal's triangle, are a special sequence of numbers defined by Italian mathematician Leonardo Fibonacci in the 13th century. In the book *Liber Abaci*, Fibonacci mentioned the question of a pair of rabbits. "If a pair of rabbits gives birth to a new pair of rabbits every month and it takes a month for the newborn pair to mature, find out how many rabbits there will be at the end of 100 months." The answer to the question was the Fibonacci sequence with the numbers 0, 1, 1, 2, 3, 5, 8, 13, 21, 34, 55, 89, 144, .... Clearly, Fibonacci sequence is a sequence of numbers where each number can be written as the sum of the two numbers that precede it. When each number after the first number in the Fibonacci number sequence is divided by the number after it, the result constantly approaches the number 0.618. The golden ratio is a geometric and numerical ratio that can be discovered between the parts of a whole, which has been applied in art and architecture, and is thought to give the dimensions that can be called the smoothest in terms of aesthetics and harmony. It is possible to encounter the golden ratio in the leaf arrangement of many plants in nature, in the ratio of each part to each other, from the anatomy of the human body to the arrangement of internal organs. When a line segment needs to be divided into two parts in accordance with the Golden Ratio, this line should be divided at such a point that the ratio of the smaller part to the larger part should be equal to the ratio of the larger part to the whole line (Markowsky, 1992).

Consider the interval  $[x_a, x_u]$  where  $x_a$  is the lower bound and  $x_u$  is the upper bound and the function has only one maximum. That is, the function is unimodal in this interval. In the golden ratio search algorithm, the search is performed by dividing the range by the golden ratio.

Let the length of the interval  $[x_a, x_u]$  be  $l_0$ . Let us divide this interval into subintervals  $l_1$  and  $l_2$  such that,  $l_0 = l_1 + l_2$  and  $\frac{l_1}{l_0} = \frac{l_2}{l_1}$

$$\frac{l_1}{l_0} = \frac{l_2}{l_1} \Rightarrow \frac{l_1}{l_1 + l_2} = \frac{l_2}{l_1}.$$

If the inverse of the equation is taken, then  $\frac{l_2}{l_1} = R$

$$1 + R = \frac{1}{R}$$

and the characteristic equation  $R^2 + R - 1 = 0$  is obtained. Looking at the roots of this equation, the positive root

$$R = \frac{\sqrt{5} - 1}{2} = 0,61803 \dots$$

gives the golden ratio.

The series given by the recurrence relation  $F_{n+1} = F_n + F_{n-1}$  for  $F_0 = 0$  and  $F_1 = 1$  for  $\forall n \geq 1$  is called the Fibonacci series. Here  $F_n$  is the  $n$ -th Fibonacci number. The ratio of two consecutive terms in the Fibonacci series;

$$0/1 = 0, 1/1 = 1, 1/2 = 0.5, 2/3 = 0.667, 3/5 = 0.6, 5/8 = 0.625, 8/13 = 0.615 \dots$$

and if continued in this way, eventually the ratio of consecutive Fibonacci numbers

$$\lim_{n \rightarrow \infty} \frac{F_{n-1}}{F_n} \cong 0,61803 \dots$$

reaches the golden ratio (Koshy, 2001).

## 2. MATERIALS AND METHODS

### 2.1. Existence of Roots for Algebraic Equations

Finding the roots of algebraic equations plays a crucial role in solving optimization problems and engineering applications. Consequently, the ability to efficiently find equation roots is a fundamental skill for mathematical modeling and solving problems in various engineering fields.

Now, let's present some basic theorems related to the existence and uniqueness of these roots, commonly found in analysis textbooks (Xue-Mei Li, David Mond, 2013).

#### **Theorem 2.1.1.** (Bolzano Theorem)

If the function  $f$  is continuous on the interval  $[a, b]$  and  $f(a) \cdot f(b) < 0$ , then there exists a  $c$  in the open interval  $(a, b)$  such that  $f(c) = 0$ .

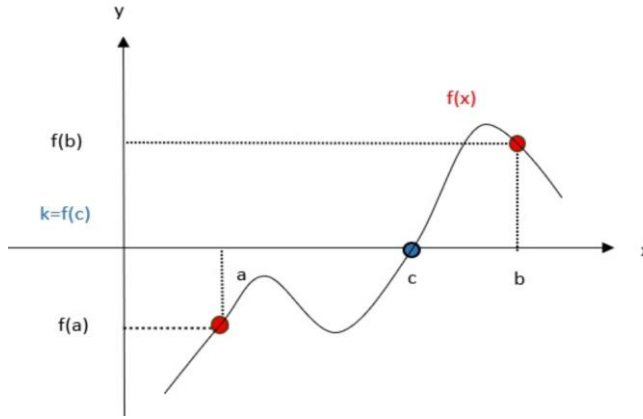


**Figure 1.** Bolzano Theorem

**Theorem 2.1.2.** If the function  $f$  is continuous, then the function  $|f|$  is continuous.

Now let us give and prove the following theorem as an obvious consequence of the above basic analysis theorems. This theorem will be used in the paper as the Root Search method in the Optimization Algorithm (Xue-Mei Li, David Mond, 2013).

**Theorem 2.1.3.** (Root Search in Optimization Algorithm)

For  $I=[a,b]$  and  $I \subset \mathbb{R}$ , if the function  $f:I \rightarrow \mathbb{R}$  is continuous, then it has at least one minima on this interval and if  $|f(x_i)| = 0$  then there exists at least one  $x_i \in I$ , ( $i \in \mathbb{N}$ ) satisfying this equality.

**Proof.** From the Extreme Value Theorem, if the function is continuous, it has at least one minima. If  $|f(x_i)| = 0$ , then  $f(x_i) = 0$ . Since this continuous function  $f$  has at least one minimum in the given closed-bounded interval and  $|f(x_i)| = 0$  this minimum takes its zero value at the roots  $x = x_i$ ,  $i \in \mathbb{N}$ , in the given interval. Thus there is at least one  $x_i \in I$ ,  $i \in \mathbb{N}$ , satisfying the equality  $f(x_i) = 0$  (Köse et al., 2024).

**2.2. Root Finding Methods**

A root-finding algorithm is a numerical method or algorithm for finding a value of  $x$  in a given function that makes the value of the function zero. There is such a point  $x$  such that  $f(x)=0$  and this  $x$  value is called the root of the function.

Consider a function  $f(x)$  in one variable. Suppose we want to solve the following linear optimization model.

$$\begin{aligned} & \text{Max } f(x) \\ & a \leq x \leq b \end{aligned}$$

For some  $x$ ,  $f'(x)$  may not exist or it may be very difficult to solve the equation  $f'(x)=0$ . How can the optimum value of the function  $f(x)$  be found if there is only one vertex in a given interval?

If  $f(x)$  is unimodal in the interval  $[a, b]$ , there is only one local maximum  $\bar{x}$  in the interval  $[a, b]$  and it is solved by the linear optimisation problem model given above.  $\bar{x}$  is the optimum solution of this model in the interval  $[a, b]$ . If  $x_1 < x_2$  at the points  $x_1$  and  $x_2$ , which are two points in the interval  $[a, b]$ , we can narrow the interval until we find the solution when we examine the function  $f(x)$ . When  $f(x_1)$  and  $f(x_2)$  are analysed, one of the following three cases occurs. In all three cases, the optimum solution is in the interval  $[a, b]$ .

**Case 1.** Since  $f(x_1) < f(x_2)$  and  $f(x)$ , is increasing in at least part of the interval  $[x_1, x_2]$ , the optimum solution cannot occur in the interval  $[a, x_1]$  due to the unimodality of  $f(x)$ . Therefore  $\bar{x} \in (x_1, b]$ .

**Case 2.** If  $f(x_1) = f(x_2)$ ,  $f(x)$  is decreasing in some part of the interval  $[x_1, x_2]$  and the optimum solution is in  $a < x_2$ . Therefore  $\bar{x} \in [a, x_2)$ .

**Case 3.** If  $f(x_1) > f(x_2)$ , then  $\bar{x} \in [a, x_2)$ .

The interval in which  $\bar{x}$  is to be found in the interval  $[a, x_2)$  or  $(x_1, b]$  is called the uncertainty interval. Many search algorithms utilise these ideas to reduce this uncertainty range.

Many of these algorithms use the following steps:

**Step 1.** Start with  $[a, b]$  as the uncertainty interval for  $x$ . Examine  $f(x)$  for reasonably chosen points  $x_1$  and  $x_2$ .

**Step 2.** Determine which of cases 1, 2 or 3 it fits and reduce the uncertainty interval accordingly.

**Step 3.** Examine  $f(x)$  for two new points (the algorithm specifies how to choose these two new points). Return to Step 2 until the uncertainty interval is small enough (Winston, 2003; Kubat, Uygun).

**Tolerance control:** Refers to repeat this process until a tolerance value is reached within a specified margin of error.

**Continuing with iterations:** Repeating steps over the newly determined range until the maximum number of iterations is reached to narrow the range.

By applying the steps in this order, the root of the function can be found by the root finding algorithms. This process, by narrowing the range containing the root at each iteration, will eventually lead to a very approximate root value (Köse et al., 2024).

If we apply the root-finding methods to the first derivative of the function as we apply them to the function itself, we identify the critical points of the function. Thus, if the function is multimodal in the given interval, these critical points are candidates for local maximum or local minimum points. If the function is unimodal, the image of this critical point is a candidate absolute maximum or absolute minimum value. Therefore, the following methods are applied to the function and then to its first derivative to find both the root of the function and its optimum value.

Let's investigate two specific approaches: the Fibonacci search algorithm and the golden ratio search algorithm.

### 2.2.1. Golden Ratio Search Algorithm

Given the function  $y = f(x)$ , let  $f$  be continuous on the interval  $[x_a, x_u]$ . Let  $x_a$  be the lower boundary and  $x_u$  be the upper boundary and the points  $x_1$  and  $x_2$  are chosen according to the golden ratio rule as follows:

$$\text{Let } x_1 = x_a + \frac{\sqrt{5}-1}{2} \cdot (x_u - x_a).$$

$$\text{Let } x_2 = x_u - \frac{\sqrt{5}-1}{2} \cdot (x_u - x_a).$$

Calculate the values of  $f(x_1)$  and  $f(x_2)$ .

If  $f(x_1) < f(x_2)$ , the search for roots in the interval  $[x_a, x_1]$  continues. Then  $x_u = x_1$  is taken.

If  $f(x_2) < f(x_1)$ , we continue to search for roots in the interval  $[x_2, x_u]$ . In this case,  $x_a = x_2$  is taken (Köse et al., 2024).

### 2.2.2. Fibonacci Search Algorithm

The Fibonacci Search Algorithm is to search an ordered sequence using Fibonacci numbers. In this algorithm, the ordered sequence to be searched is divided into parts based on Fibonacci numbers. Research on Fibonacci numbers and the performance of this algorithm has an important place in computer science.

The Fibonacci Search Algorithm works as follows:

1. It is checked whether the sequence to be searched is greater or less than the largest Fibonacci number.
2. If the number to be searched is smaller, the previous Fibonacci number is added to the current number.
3. This process continues from the largest range to the smallest, narrowing the range.
4. Finally, when the range is reduced to 1, the number is found (or not found if the number is not in the series) (Köse et al., 2024).

## 3. PERFORMANCE MEASURES AND RESULTS

### 3.1. Test Functions and Simulation Graphs

Three different functions were used to test the Golden Ratio search algorithm and Fibonacci search algorithms used to find the root of univariate algebraic functions. The test functions are respectively defined with the intervals given next to them

$$f(x) = x^4 + x^3 - 7x^2 - x + 6, \quad [-3.5, 3.5]$$

$$g(x) = \cos x - \frac{x^3}{5}, \quad [-3.5, 3.5]$$

$$h(x) = \log(x^2 + 1.5x + 1), \quad [-3.5, 3.5]$$

will be considered. The graphs of these functions are given in Figure 2.

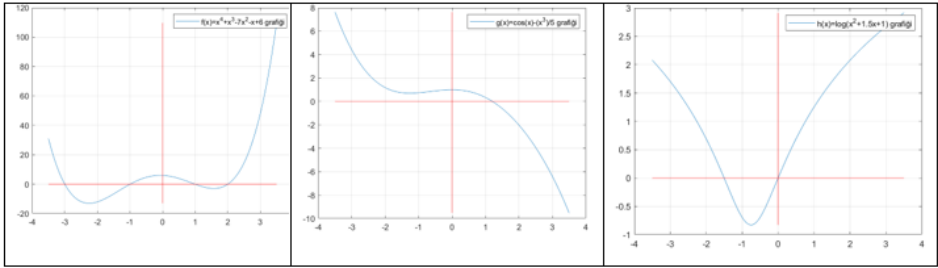


Figure 2. Graphs of the functions  $f$ ,  $g$  and  $h$

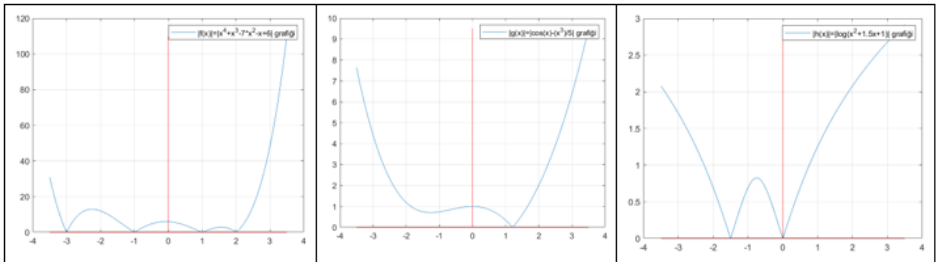


Figure 3. Graphs of  $|f|$ ,  $|g|$  and  $|h|$  functions

### 3.1.1. Simulation Graphs of Approaching the Minimum Value with the Golden Ratio Search Algorithm

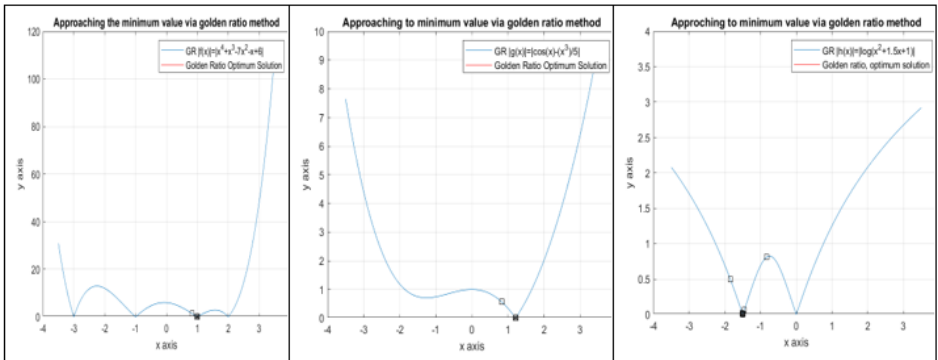
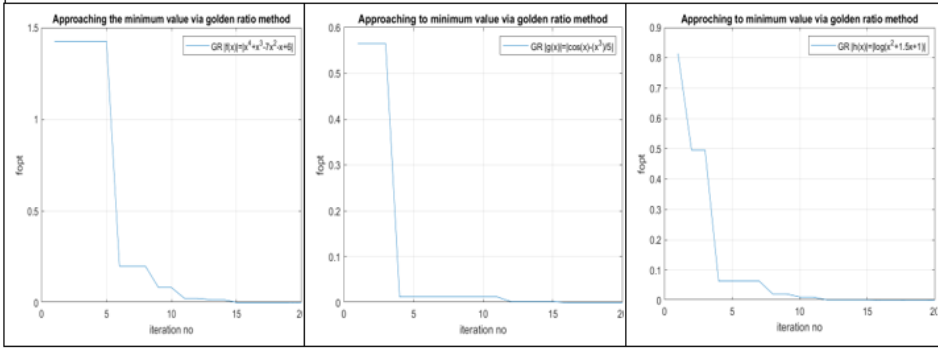
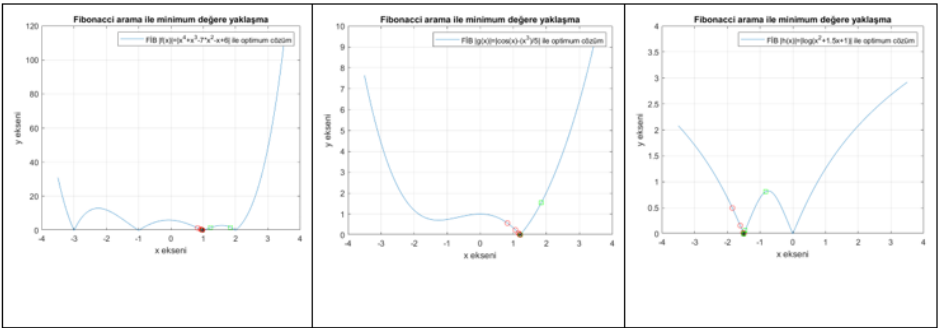


Figure 4. Graphs of  $|f|$ ,  $|g|$  and  $|h|$  functions approaching the minimum value with the Golden Ratio Search method

Figure 5 shows the speed at which the functions  $|f|$ ,  $|g|$  and  $|h|$  approach the minimum value using the Golden Ratio Search Algorithm with the number of iterations.



**Figure 5.** Speed of approaching the minimum value of  $|f|$ ,  $|g|$  and  $|h|$  functions with the Golden Ratio Search method (number of iterations)



**Figure 6.** Approximation graphs of  $|f|$ ,  $|g|$  and  $|h|$  functions to the minimum value with Fibonacci Search method

### 3.1.2. Graphs of Simulated Approach to Minimum Value with Fibonacci Search Algorithm

Figure 7 shows the speed of approaching the minimum value of the  $|f|$ ,  $|g|$  and  $|h|$  functions using the Fibonacci Search Algorithm with the number of iterations.

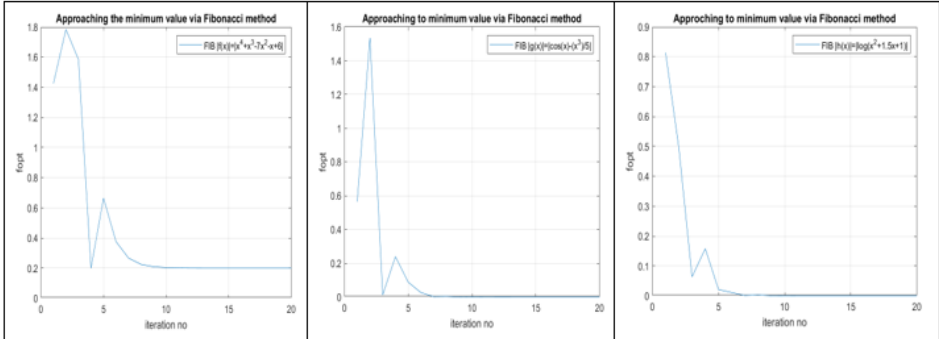


**Figure 7.** Speed of approaching the minimum value of  $|f|$ ,  $|g|$  and  $|h|$  functions with Fibonacci Search method (number of iterations)

### 3.1. Error Accounts in Performance Evaluation

The problem of finding the root of algebraic equations is a fundamental element of numerical analysis and computer science. In this study, the approximate values obtained by numerical and optimization methods and the difference between these values and the actual values, i.e. the error values, are of critical importance. This section discusses the equations representing the errors and finally presents the computational results of these errors for performance evaluation of the algorithms.

#### 3.1.1. Mean absolute error (MAE)

Mean absolute error (MAE) is frequently used in regression and time series problems because it is easy to interpret. MAE is a measure of the difference between two continuous variables, i.e. the average of the absolute values of the differences between actual and predicted values, and measures the magnitude of deviations between predictions and actual values. (Chai & Draxler, 2014). (Chai, T., & Draxler, R. R. (2014). The Mean Absolute Error formula is given by the formula in Equation (1)

$$\text{MAE} = \frac{1}{n} \sum_{i=1}^n |x_g - x_i| \quad (1)$$

where  $x_g$ : real root,  $x_i$ : approximate root obtained at step  $i$ ,  $n$ : total number of iterations.

### 3.1.2. Mean Absolute Approximation Error (MAAE)

Mean Absolute Approximation Error (MAAE) is a type of error used to determine how accurate these approximations are when the true value of a given quantity is unknown but can be approximated. It is usually calculated as the average of the absolute values of the difference between the values obtained at each step in an iteration process and the values calculated at the previous step. This error measure is commonly used to assess how accurate an estimate is, especially in numerical analysis, optimization, and engineering. Mean Absolute Error of Approximation is often used in computational processes or modeling operations. For example, at each step of an iterative algorithm, the average value of the difference between the values obtained and the values calculated in the previous step can be calculated to evaluate how accurate and stable this algorithm works. Furthermore, this error measure can be used in various scientific research and experiments to assess how insignificant the difference between measurements is. In this way, it provides information about the accuracy and reliability of the data and increases the credibility of the results. The mean absolute error of approximation is given in Equation (2) where

$x_i$ : approximate root obtained in step  $i$ ,

$k$ : number of iterations with minimum error

$$MAAE = \frac{1}{k} \sum_{i=0}^k \left| \frac{x_{i+1} - x_i}{x_{i+1}} \right| \quad (2)$$

While calculating the Mean Absolute Approximate Error throughout this study, since the root  $x_{i+1}$  in the denominator of Equation (2) is zero in some cases, this term will be ignored in order to avoid undefinedness and the Mean Absolute Approximate Error will be calculated with the formula given in Equation (3).

$$MAAE = \frac{1}{k} \sum_{i=0}^k |x_{i+1} - x_i| \quad (3)$$

### 3.2. Analysis and Comparison

Since it is necessary to consider both error values and error reduction rate when evaluating algorithm effectiveness, especially for complex problems and large data sets, simulations are performed for the test functions selected here. The test set is compared by finding the optimal roots of the selected test functions for each algorithm, and this comparison is evaluated with the performance metrics Mean Absolute Error (MAE) and Mean Absolute Approximation Error (MAAE). Since it is expected to achieve a level of precision using a minimum of iterations and computational resources, the algorithms' estimates are evaluated with the following performance metrics.

The rate of convergence to the minimum value, optimum points and global minimum values of the nonlinear test functions used in the testing phase are given in the table below and absolute errors are calculated.

In the table below,  $i$  is the number of iterations,  $f, g$  and  $h$  are the test functions,  $x_f, x_g$  ve  $x_h$  are the real roots of  $f, g$  and  $h$  respectively,  $optx_f, optx_g$  and  $optx_h$  indicate the optimum points of the functions  $f, g$  and  $h$  respectively, and  $opty_f, opty_g$  ve  $opty_h$  indicate the optimum values of the functions  $f, g$  and  $h$  respectively. In the table, various statistics such as best solution, optimum solution, absolute error, average absolute error, average absolute approximation error, average absolute error depending on the number of iterations and average absolute approximation error depending on the number of iterations are presented for the Golden Ratio algorithm (GR) and Fibonacci Search Algorithm (FIB).

**Table 1.** Absolute errors of test functions

Test Functions	Statistics	GR	FIB
<b><i>f</i></b> <b>Real roots</b> $x_1 = -3$ $x_2 = -1$ $x_3 = 1$ $x_4 = 2$	<i>i</i>	20	4
	$x_f$	1	1
	$optx_f$	0.99995	0.9752
	$opty_f$	0.0002	0.1992
	Absolute error	0	0.0248
	Average absolute error	0.0487	0.0875
	Average absolute error depending on the number of iterations	0.0487	0.3156
	Average absolute approximation error	0.0102	0.2238
	Average absolute approximation error depending on the number of iterations	0.9163	1.0585
<b><i>g</i></b> <b>Real roots</b> $x_1 = 1.2091$	<i>i</i>	17	9
	$x_g$	1.2091	1.2092
	$optx_g$	1.2092	1.2092
	$opty_g$	0.0001	0.0001
	Absolute error	0	0
	Average absolute error	0.0606	0.0620
	Average absolute error depending on the number of iterations	0.0712	0.1375
	Average absolute approximation error	0.02	0.2355
	Average absolute approximation error depending on the number of iterations	1.0777	0.4806
<b><i>h</i></b> <b>Real roots</b> $x_1=0$ $x_1 = -1.5$	<i>i</i>	20	11
	$x_h$	-1.5	-1.5
	$optx_h$	-1.5	-1.5
	$opty_h$	0	0
	Absolute error	0	0
	Average absolute error	0.0794	0.0598
	Average absolute error depending on the number of iterations	0.0794	0.1087
	Average absolute approximation error	0.0750	0.1
	Average absolute approximation error depending on the number of iterations	0.9163	0.3933

For the function  $f$ , FIB reached the lowest absolute error value (0.0248) with the lowest number of iterations (4 iterations), while the GR method reached the lowest average absolute error (0.00005) at higher iterations (20 iterations). Again, when the average absolute errors depending on the number of iterations for the function  $f$  are compared, it is seen that the GR method produces more accurate results ( $0.0487 < 0.0875$ ). When the average absolute approximation errors are considered, it is seen that the GR method gives the most successful result ( $0.0102 < 0.2238$ ). It is also seen that the GR method gives more successful results in the average absolute approximation error depending on the number of iterations ( $0.9163 < 1.0585$ ). In summary, it is seen that the GR method is more accurate and more successful than the FIB method in all error calculations.

For the function  $g$ , GR and FIB methods have very close average absolute error (GR)  $0.0606 < 0.0620$  (FIB), while FIB has the least number of iterations (9 iterations). Regarding the mean absolute approximation errors, GR method achieved the most accurate result ( $0.02 < 0.2355$ ). While the average absolute error based on the number of iterations reached the most successful result with GR, the average absolute approximation error based on the number of iterations reached the most precise value with the FIB method 0.4806. For the function  $g$ , the FIB method is more successful than the GR method with the fewest iterations and the average absolute approximation error based on the number of iterations. This shows that the performance of the algorithms may vary for different function types.

In the tests on the function  $h$ , the FIB method has the lowest mean absolute error (0.0598) but the highest mean absolute approximation error (0.1) with 11 iterations. GR is again a successful method in the calculation of the average absolute error according to the number of iterations (0.0794), while the FIB method gives the best result in the calculation of the average absolute approximation error according to the number of iterations (0.3933).

#### **4. CONCLUSION AND EVALUATION**

The results given in Table 1 show that the performance of different optimization algorithms on various test functions may vary and that the choice of the optimal root-finding method should be carefully considered depending on the specific problem situation.

According to these results, both methods have advantages and disadvantages in certain situations. Below are some observations based on the test functions and the results obtained:

**Golden Ratio Search (GR).** The GR method is notable for the lowest absolute errors (0.00) for the functions  $f$ ,  $g$  and  $h$ . It shows that the GR method can be effective for these types of functions. Considering the average absolute errors, it was observed that they were 0.0487, 0.0606 and 0.0794 for the functions  $f$ ,  $g$  and  $h$ , respectively. Considering the mean absolute approximation errors, the results are 0.0102, 0.02 and 0.0750 for the functions  $f$ ,  $g$  and  $h$ , respectively. Accordingly, the GR method gives mostly successful results in the calculation of the mean absolute error. In the mean absolute approximation error calculation, it performs the best in all three functions.

**Fibonacci Search (FIB).** The FIB method shows that it can provide faster results compared to the GR method with minimum iterations for all functions. The FIB method generally gives better results in the calculation of the average absolute approximation error depending on the number of iterations. This shows that Fibonacci search can be advantageous for specific problems.

In general, the performance of each method varies depending on the properties of the function under test. This shows that the properties of the function should be carefully analyzed when choosing an optimal root-finding method. In addition, other factors such as the number of iterations and the precision of approximating the root of each method should also be taken into account. The differences between the methods are due to the approximation strategies and mathematical structures of the algorithms, so it is important to choose the method that best suits the nature of a particular problem.

## REFERENCES

- [1] Chai, T. and Draxler, R.R. (2014) Root Mean Square Error (RMSE) or Mean Absolute Error (MAE)? Arguments against Avoiding RMSE in the Literature. *Geoscientific Model Development*, 7, 1247-1250. <http://dx.doi.org/10.5194/gmd-7-1247-2014>
- [2] Gemechu T., Thota S., 2020, On New Root Finding Algorithm for Solving Nonlinear Transcendental Equations, *International Journal of Chemistry, Mathematics and Physics (IJCMP)*, 4(2), 18-24.
- [3] Koshy T., 2001. *Fibonacci and Lucas numbers with applications*, Wiley, New York.
- [4] Köse, B., Demirtürk, B., & Konca, Ş. (2024). An Application on Performance Analysis of Fibonacci and Golden Ratio Algorithms in Root Finding Methods. 1st International Conference on Experimental and Computational Engineering Sciences - ICECES 2024, May 30-31, 2024, University of Turkish Aeronautical Association, Ankara, Türkiye.
- [5] Kubat C., Uygun Ö., *Yöneylem Araştırması 3 Ders Notları*.
- [6] Markowsky G., 1992. Misconceptions about the Golden Ratio, *The College Mathematics Journal*, 23(1), 2-19.
- [7] Sabharwa C. L., 2019. Blended Root Finding Algorithm Outperforms Bisection and Regula Falsi Algorithms, *Mathematics*, 7, 1118; doi:10.3390/math7111118.
- [8] Semenov V. Yu., 2015. A Method to Find all the Roots of the System of Nonlinear Algebraic Equations Based on the Krawczyk Operator, *Cybernetic and Systems Analysis*, 51(5), 819-825.
- [9] Thota S., 2019. A new root finding algorithm using exponential series, *Ural Mathematical Journal* 5(1), 83-90.
- [10] Vatanserver F., Hatun M., 2015. Newton Tabanlı Kök Bulma Yöntemleri için Simülasyon Tasarımı, *SAÜ Fen Bil. Der.*, 19(3), 327-337.
- [11] Wayne Winston, 2003. *Operations Research Applications and Algorithms* 4th. Edition.
- [12] Xue-Mei Li, David Mond, 2013. *Lecture Notes for Analysis II*.

## A Savings Model under Nonlocal Boundary Conditions<sup>1</sup>

Olgun CABRİ<sup>2</sup>, Hanlar REŞİDOĞLU<sup>3</sup>

### 1. Introduction

In recent years, the solutions to many physical phenomena have been modeled by non-classical parabolic or hyperbolic initial–boundary value problems involving integral terms. These integrals may appear either within the structure of the partial differential equation itself or in its boundary conditions [7].

Nonlocal boundary conditions establish relationships between the values of a solution or its derivatives at distinct boundary points or interior locations within the domain. Boundary conditions expressed in integral form can be regarded as a special case of such nonlocal conditions [13].

Problems of this nature arise in various applied fields, including chemical diffusion, heat conduction, thermoelasticity, population dynamics, vibration analysis, nuclear reactor processes, and several biological systems [7].

A large number of physical problems in which classical boundary conditions are replaced by integral ones are associated with wave or diffusion-type equations (see [2,3,8,9,10]).

Numerous numerical studies have been conducted on problems involving integral boundary conditions [3,4,5,7,11,14].

In this study, a family savings model used in the field of economics is examined. The model is described by a diffusion equation subject to integral boundary conditions. This study aims to reduce the diffusion model with integral boundary conditions to a Sturm–Liouville form and to derive the eigenvalues and eigenfunctions for an explicit expression of the solution.

---

<sup>1</sup> This paper originates from the Ph.D. dissertation of Dr. Olgun Cabri, supervised by Prof. Dr. Hanlar Reşidoğlu.

<sup>2</sup> Asst. Prof., Artvin Coruh University, Department of Business Management, Hopa, 08600, Artvin, Turkey,  
Email: olguncabri@artvin.edu.tr Orcid: 0000-0002-0690-9667

<sup>3</sup> Prof. Dr., Iğdir University, Department of Mathematics, 76000, Iğdir, Turkey,  
Email: hanlar.residoglu@igdir.edu.tr, Orcid: 0000-0002-3283-9535

## 2. Family Saving Model

The family saving model, originally introduced in [6], describes the income level of a family at a given point in time as follows:

$$dx = \Phi(x, t)dt + \Gamma(x, t)dX, \quad G \geq 0 \quad (1)$$

In this equation,  $\Phi(x, t)$  denotes a specific function representing the difference between a family's income and expenditures, and thus the rate of saving. The term  $\Gamma(x, t)$  represents the random fluctuation of income. If this equation is generalized to describe the saving behavior of all families in society, disregarding the dynamics of individual households, the function  $p(x, t)$ , which represents the density distribution of family savings, satisfies the following diffusion-type partial differential equation:

$$\frac{\partial p}{\partial \tau} = -\frac{\partial}{\partial \xi}((c + \Phi)p) + \frac{1}{2} \frac{\partial^2}{\partial \xi^2} (bp) + g.$$

In the literature, such equations are generally referred to as Kolmogorov-type equations. We consider this equation with initial condition

$$p(\xi, 0) = \psi(\xi), \quad 0 \leq x \leq l \quad (2)$$

and with boundary conditions

$$\int_0^l p(\xi, t) d\xi = M(t), \quad t \geq 0, \quad (3)$$

$$\int_0^l \xi p(x, t) d\xi = Q(t), \quad t \geq 0. \quad (4)$$

Here,  $M_0(t)$  denotes the number of families within the interval, while  $Q_0(t)$  represents the total amount of savings [6].

## 3. Problem

Let us consider the following non-homogeneous problem defined in the region  $D = \{(\xi, t): 0 < \xi < 1, 0 < \tau < T\}$  subject to two nonlocal boundary conditions:

$$\frac{\partial p}{\partial \tau} = \alpha^2 \frac{\partial^2 p}{\partial \xi^2} + g(\xi, \tau), \quad (5)$$

$$p(\xi, 0) = \psi(\xi), \quad (6)$$

$$\int_0^1 p(\xi, t) d\xi = M(\tau), \quad (7)$$

$$\int_0^1 \xi p(\xi, \tau) d\xi = Q(\tau). \quad (8)$$

The functions  $g(\xi, \tau)$ ,  $M(\tau)$ ,  $Q(\tau)$  and  $\psi(\xi)$  are assumed to be defined on the region  $D$  and to be continuously differentiable. For a solution, the following compatibility conditions must be satisfied:

$$\int_0^1 \xi \psi(\xi) d\xi = M(0), \quad \int_0^1 \psi(\xi) d\xi = Q(0).$$

Implementing the substitution,

$$p(\xi, \tau) = (\xi, \tau) + (12Q(\tau) - 6M(\tau))\xi + 4M(\tau) - 6Q(\tau).$$

The given boundary-value problem is transformed into

$$\frac{\partial \rho}{\partial t} = \alpha^2 \frac{\partial^2 \rho}{\partial \xi^2} + G(\xi, \tau), \quad (9)$$

$$\rho(\xi, 0) = \psi(\xi), \quad (10)$$

$$\int_0^1 \rho(\xi, t) d\xi = 0, \quad (11)$$

$$\int_0^l \xi \rho(x, t) d\xi = 0, \quad (12)$$

Where

$$G(\xi, \tau) = g(\xi, \tau) - (12Q'(\tau) - 6M'(\tau))\xi + 4M'(\tau) - 6Q'(\tau)$$

$$\varphi(\xi) = \psi(\xi) - (12Q(0) - 6M(0))\xi + 4M(0) - 6Q(0).$$

Due to linearity of problem (11-12), the solution can be represented as the superposition of the solutions corresponding to two separate boundary value problems. The first problem is given by

$$\frac{\partial \rho}{\partial \tau} = \alpha^2 \frac{\partial^2 \rho}{\partial \xi^2}, \quad (13)$$

$$\rho(\xi, 0) = \psi(\xi), \quad (14)$$

$$\int_0^1 \rho(\xi, \tau) d\xi = 0, \quad (15)$$

$$\int_0^1 \xi \rho(\xi, \tau) d\xi = 0,, \quad (16)$$

the second problem is described by

$$\frac{\partial \rho}{\partial \tau} = \alpha^2 \frac{\partial^2 \rho}{\partial \xi^2} + G(\xi, \tau), \quad (17)$$

$$\rho(\xi, 0) = 0, \quad (18)$$

$$\int_0^1 \rho(\xi, \tau) d\xi = 0, \quad (19)$$

$$\int_0^1 \xi \rho(\xi, \tau) d\xi = 0. \quad (20)$$

If  $\rho_1(\xi, \tau)$  is the solution of the boundary value problem (13)–(16) and  $\rho_2(\xi, \tau)$  is the solution of the boundary value problem (17)–(20), then the solution of the boundary value problem (9)–(12) is given by the sum

$$\rho(\xi, \tau) = \rho_1(\xi, \tau) + \rho_2(\xi, \tau).$$

Let us transform the nonlocal boundary conditions (15)–(16) into their equivalent local forms. By (17), we get

$$\begin{aligned} \int_0^1 \rho_\tau(\xi, \tau) d\xi &= \alpha^2 \int_0^1 \rho_{\xi\xi}(\xi, \tau) d\xi, \\ \Rightarrow \frac{d}{d\tau} \left( \int_0^1 \rho(\xi, \tau) dx \right) &= \alpha^2 \int_0^1 \rho_{\xi\xi}(\xi, \tau) d\xi, \\ \Rightarrow 0 &= \alpha^2 \int_0^1 \xi \rho_{\xi\xi}(\xi, \tau) d\xi. \end{aligned}$$

Using integration by parts, one obtains

$$\rho_\xi(1, \tau) - \rho_\xi(0, \tau) = 0.$$

If we apply a similar procedure to the other boundary condition, we obtain:

$$\begin{aligned} \int_0^1 \xi \rho_\tau(\xi, \tau) d\xi &= \alpha^2 \int_0^1 \xi \rho_{\xi\xi}(\xi, \tau) d\xi \\ \Rightarrow \frac{d}{d\tau} \left( \int_0^1 \xi \rho_{t\tau}(\xi, \tau) d\xi \right) &= \alpha^2 \int_0^1 \xi \rho_{\xi\xi}(\xi, \tau) d\xi \\ \Rightarrow 0 &= \alpha^2 \int_0^1 \xi \rho_{\xi\xi}(\xi, \tau) d\xi \end{aligned}$$

Thus, by integration by parts we get

$$\rho_\xi(1, \tau) - \rho(1, \tau) + \rho(0, \tau) = 0.$$

Hence, the boundary value problem (13)–(16) is transformed into the equivalent local problem:

$$\frac{\partial \rho}{\partial \tau} = \alpha^2 \frac{\partial^2 \rho}{\partial \xi^2}, \quad (21)$$

$$\rho(\xi, 0) = \psi(\xi), \quad (22)$$

$$\rho_\xi(1, \tau) - \rho_\xi(0, \tau) = 0, \quad (23)$$

$$\rho_\xi(1, \tau) - \rho(1, \tau) + \rho(0, \tau) = 0. \quad (24)$$

Using Fourier method,

$$\rho(\xi, \tau) = Y(\xi)Z(\tau)$$

we obtain following Sturm Liouville problem

$$Y''(\xi) + \lambda Y(\xi) = 0, \quad (25)$$

$$Y'(1) - Y'(0) = 0, \quad (26)$$

$$Y'(1) - Y(1) + Y(0) = 0, \quad (27)$$

and differential equation

$$Z'(\tau) + \alpha^2 Z(\tau) = 0. \quad (28)$$

It is well known from [12] that the boundary conditions (26)-(27) are regular. So the eigenfunctions of the problem form a Riesz basis.

#### 4. Analysis of Eigenvalues and Eigenfunctions

Let us investigate the eigenvalues and eigenfunctions of the Sturm–Liouville equations (25)–(27). Let  $\lambda = \mu^2$ .

- When  $\lambda = \mu^2 < 0$ , the problem possesses only the trivial solution..
- For  $\lambda = 0$  the problem has a double eigenvalue, and the corresponding solution is of the form

$$Y_0(\xi) = A_0 + B_0 \xi.$$

The eigenfunctions corresponding to this eigenvalue are

$$Y_{0,1}(\xi) = 1, Y_{0,2}(x) = \xi.$$

- For  $\lambda = \mu^2 > 0$ , In this case, the solution takes the form
- 

$$Y(\xi) = a_1 \cos \sqrt{\mu} \xi + a_2 \sin \sqrt{\mu} \xi.$$

By applying boundary condition (26) to the obtained solution, we get

$$- \sin \sqrt{\mu} a_1 + (\cos \sqrt{\mu} - 1) a_2 = 0.$$

Next, by applying boundary condition (27), we obtain

$$(1 - \cos \sqrt{\mu} - \sqrt{\mu} \sin \sqrt{\mu}) a_1 + (\sqrt{\mu} \cos \sqrt{\mu} - \sin \sqrt{\mu}) a_2 = 0.$$

Hence, the characteristic equation takes the form

$$\Delta = 2 - 2 \cos \sqrt{\mu} - \sqrt{\mu} \sin \sqrt{\mu} = 0.$$

If we set  $\sqrt{\mu} = r$  in the characteristic equation, it can be rewritten as

$$\Delta = 2 - 2 \cos r - r \sin r = 0. \quad (29)$$

Applying the half-angle identities for sine and cosine to equation (29), the characteristic equation becomes as

$$\begin{aligned} \Rightarrow \Delta &= 2 - 2r \sin \frac{r}{2} \cos \frac{r}{2} - 2(1 - 2 \sin^2 \frac{r}{2}) = 0, \\ \Rightarrow \Delta &= \sin \frac{r}{2} \left( r \cos \frac{r}{2} - \sin \frac{r}{2} \right) = 0. \end{aligned}$$

One of the roots of this equation satisfies the condition  $\sin(r/2) = 0$ , and it is easily seen that these roots are given by

$$r_{2m} = 2\pi m, m = 1, 2, \dots \quad (30)$$

The remaining roots are obtained from the equation:

$$r \cos \frac{r}{2} - \sin \frac{r}{2} = 0 \Rightarrow \tan \left( \frac{r}{2} \right) = \frac{r}{2}.$$

These roots satisfy  $r_{2m+1} \in \left[ 2\pi m + \frac{\pi}{2}, (2m+1)\pi \right]$ . Let us derive an asymptotic formula. Let  $r_{2m} = (2m+1)\pi - \varepsilon$ . Following [1], we apply the Lagrange inversion formula.

Thus we have

$$\begin{aligned} \frac{2 \cos(\varepsilon) + \varepsilon \sin(\varepsilon) + 2}{\sin(\varepsilon)} &= (2m+1)\pi = k^{-1}, \\ \Rightarrow \frac{\varepsilon}{\varepsilon \left( \frac{2 \cos(\varepsilon) + \varepsilon \sin(\varepsilon) + 2}{\sin(\varepsilon)} \right)} &= k, \\ \Rightarrow \varepsilon &= \frac{(2m+1)\pi}{2} - c_1 \left( \frac{(2m+1)\pi}{2} \right)^{-1} - c_2 \left( \frac{(2m+1)\pi}{2} \right)^{-3} \dots \end{aligned}$$

Where

$$c_j = \frac{1}{j!} \left\{ \left( \frac{d}{d\varepsilon} \right)^{j-1} h(\varepsilon)^j \right\} \Bigg|_{\varepsilon=0}, \quad h(\varepsilon) = \varepsilon \left( \frac{2 \cos(\varepsilon) + \varepsilon \sin(\varepsilon) + 2}{\sin(\varepsilon)} \right).$$

Once the coefficients  $c_j$  are evaluated, the roots are found asymptotically as

$$r_{2m+1} = (2m+1)\pi - 4((2m+1)\pi)^{-1} - \frac{32}{3}((2m+1)\pi)^{-3} - \frac{832}{15}((2m+1)\pi)^{-5} + O\left(\frac{1}{m^7}\right).$$

Thus, the eigenfunctions corresponding to these eigenvalues are obtained as

$$Y_{2m} = \cos(2\pi m)\xi, \\ Y_{2m+1} = \sin\left(r_{2m+1}\left(\frac{1}{2} - \xi\right)\right).$$

The norms of these eigenfunctions are given by

$$\|Y_{0,1}(\xi)\|^2 = 1, \quad \|Y_{0,2}(\xi)\|^2 = 1/\sqrt{3}, \\ \|Y_{2m}(\xi)\|^2 = \int_0^1 \cos(2\pi m\xi)^2 d\xi = \frac{1}{2} + \frac{\sin(4\pi m\xi)}{8\pi m} \Bigg|_0^1 = \frac{1}{2}, \\ \|Y_{2m+1}(\xi)\|^2 = \frac{1}{2} - \frac{\sin r_{2m+1}}{r_{2m+1}}.$$

The solution to problem (28) is expressed as

$$Z(\tau) = C_n e^{\alpha^2 r_m^2 \tau}.$$

As a result, the solution of problem (13)–(16) is obtained as

$$\rho_1(\xi, \tau) = A_0 + A_1 \xi + \sum_{m=1}^{\infty} A_{2m} \cos(2\pi m\xi) e^{-\alpha^2 4\pi^2 m^2 \tau} + \sum_{m=1}^{\infty} B_m \left( \sin\left(r_{2n+1}\left(\frac{1}{2} - \xi\right)\right) \right) e^{-\alpha^2 r_m^2 \tau}.$$

In this expression, the coefficients take the form

$$\begin{aligned}
 A_0 &= \int_0^1 \psi(\xi) d\xi, \\
 A_1 &= 3 \int_0^1 \xi \psi(\xi) d\xi - \frac{1}{2} A_0, \\
 A_{2m} &= 2 \int_0^1 \psi(\xi) \cos(2\pi m) \xi d\xi, \quad m = 1, 2, \dots \\
 B_{2m} &= \frac{1}{\|Y_{2m+1}(\xi)\|^2} \int_0^1 \psi(\xi) \left( \sin \left( r_{2m+1} \left( \frac{1}{2} - \xi \right) \right) \right) d\xi, \quad m = 1, 2, \dots
 \end{aligned}$$

For the solution of the nonhomogeneous boundary value problem (17)–(20), if the function  $G(x, t)$  is expanded in terms of the eigenfunctions, we get

$$G(\xi, t) = \sum_{n=0}^{\infty} C_n(t) Y_{2n}(\xi) + D_n(t) Y_{2n+1}(\xi).$$

Hence the solution of (21-24) is obtained by

$$\begin{aligned}
 \rho_2(\xi, t) &= \sum_{n=0}^{\infty} \left[ \int_0^t C_n(\tau) e^{-\alpha^2(2n\pi^2)(t-\tau)} d\tau \right] Y_{2m}(\xi) \\
 &\quad + \left[ \int_0^t D_n(\tau) e^{-\alpha^2 r_n^2(t-\tau)} d\tau \right] Y_{2m+1}(\xi),
 \end{aligned}$$

Where

$$\begin{aligned}
 C_n(\tau) &= 2 \int_0^{\tau} G(\xi, \tau) Y_{2n}(\xi) d\xi, \\
 D_n(\tau) &= \frac{1}{\|Y_{2m+1}(\xi)\|^2} \int_0^1 G(\xi, \tau) Y_{2n+1}(x) d\xi.
 \end{aligned}$$

## 5. Example

Let us consider the following PDE modeling the density of family savings in the region  $D = \{(\xi, t): 0 < \xi < 1, 0 < t < T\}$

$$\begin{aligned}\frac{\partial \rho}{\partial \xi} &= \alpha^2 \frac{\partial^2 \rho}{\partial \xi^2} + f(\xi, \tau), \\ \rho(\xi, 0) &= \varphi(\xi), \\ \int_0^1 \rho(\xi, t) dx &= M_0, \\ \int_0^1 \xi \rho(\xi, t) d\xi &= Q_0.\end{aligned}$$

In this problem, the total number of families and the total savings are assumed to be constant. The solution of this problem is given by

$$\rho(\xi, \tau) = u(\xi, \tau) + (12Q_0 - 6M_0)\xi + 4M_0 - 6Q_0.$$

Here, since the function  $u(\xi, \tau)$  tends to zero as time progresses, it follows that as  $\tau \rightarrow \infty$

$$\rho(\xi, \tau) = (12Q_0 - 6M_0)\xi + 4M_0 - 6Q_0$$

That is, as time progresses, the distribution evolves into a linear profile. Here, if the average saving  $Q_0/M_0 > 1/2$ , the slope becomes positive, indicating that the saving shifts toward families with higher savings. Conversely, if the average saving  $Q_0/M_0 < 1/2$ , the slope becomes negative, and the distribution shifts toward families with lower savings. When the average saving equals  $Q_0/M_0 = 1/2$ , the slope is zero, and the distribution becomes uniform, representing an equal level of savings throughout.

## 6. Reference

1. Bruijn, N. G. *Asymptotic Methods in Analysis*. Dover Publications, 1970.
2. Cannon, J. R. The solution of the heat equation subject to the specification of energy. *Quart. Appl. Math.*, 1963, 21(2): 155–160.
3. Cannon, J. R.; Esteva, S. P.; Van Der Hoek, J. A Galerkin procedure for the diffusion equation subject to the specification of mass. *SIAM Journal on Numerical Analysis*, 1987, 24(3): 499–515.
4. Cannon, J. R.; Lin, Y.; Shingmin, W. An implicit finite difference scheme for the diffusion equation subject to mass specification. *International Journal of Engineering Science*, 1990, 28(7): 573–578.
5. Cannon, J. R.; Matheson, A. L. A numerical procedure for diffusion subject to the specification of mass. *International Journal of Engineering Science*, 1993, 31(3): 347–355.
6. Erofeenko, V. T.; Kozlovski, I. Y. *Partial Differential Equation and Mathematical Models in Economic*. URRS, 2011.
7. Fairweather, G.; Saylor, R. D. The reformulation and numerical solution of certain nonclassical initial-boundary value problems. *SIAM Journal on Scientific and Statistical Computing*, 1991, 12(1): 127–144.
8. Ionkin, N. I. Solution of a boundary-value problem in heat conduction with a nonclassical boundary condition. *Differential Equations*, 1977, 13(2): 294–304.
9. Ionkin, N. I.; Moiceev, E. I. Solution of boundary value problem in heat conduction theory with nonlocal boundary conditions. *Differential Equations*, 1977, 13(2): 294–304.
10. Kamynin, L. I. A boundary value problem in the theory of heat conduction with a nonclassical boundary condition. *USSR Computational Mathematics and Mathematical Physics*, 1964, 4(6): 33–59.
11. Lin, Y. *Parabolic partial differential equation subject to nonlocal boundary conditions*. Ph.D. Thesis, 1988.
12. Naimark, M. A. *Linear Differential Operators: Elementary Theory of Linear Differential Operators*. F. Ungar Publishing Company, 1968.
13. Samarskii, A. Some problems in differential equation theory. *Differential Equations*, 1980, 16(11): 1221–1228.
14. Shingmin, W.; Lin, Y. A numerical method for the diffusion equation with nonlocal boundary specifications. *International Journal of Engineering Science*, 1990, 28(6): 543–546.

# Kamada-Kawai Algorithm: A Comprehensive Analysis from Global Graph Layout to Modern Challenges

Ümit SARP<sup>1</sup>, Bilal DEMİR<sup>2</sup>

### Abstract

Graph drawing plays a critical role in transforming complex relational data into understandable visual representations. Among force-directed algorithms, the Kamada-Kawai (KK) algorithm, introduced in 1989, stands out by preserving the global structure and symmetry, using graph-theoretic shortest path distances to determine ideal distances between nodes. This article explains the mathematical foundations and energy minimization principle of the Kamada-Kawai algorithm. Its primary application areas, such as Social Network Analysis (SNA), Bioinformatics, and Software Engineering, are examined in detail. A Social Network Analysis case study is presented on a randomized "small-world" graph using the `networkx` library. Furthermore, the algorithm's performance on special topological structures like Polygonal Cycle Graphs and Dendrimer Graphs is analyzed with Python code examples. Finally, the algorithm's fundamental limitations, such as its high computational cost, its challenges, and modern approaches to these problems, like Multilevel algorithms, are discussed comprehensively.

**Keywords:** Kamada-Kawai, Graph Drawing, Force-Directed Algorithms.

---

<sup>1</sup>Lec. Dr., Continuing Education Application and Research Center, İzmir Kâtip Çelebi University, 35620 İzmir, Türkiye, 0000-0002-1260-785X, umitsarp@ymail.com, umit.sarp@ikeu.edu.tr

<sup>2</sup>Assoc Prof., Department of Mathematics, Necatibey Faculty of Education, Balıkesir University, 10100 Balıkesir, Türkiye, 0000-0002-6638-69092, bdemir@balikesir.edu.tr

## 1. Introduction

Relational data is one of the cornerstones of modern science. In many fields, from social networks to biological systems, and from software architecture to logistics networks, entities and the relationships between them are most naturally modeled as graphs [1-3]. When these graphs contain thousands of nodes, raw data tables make the complex structures they contain incomprehensible to human perception. At this point, graph drawing, or data visualization, plays a critical role by transforming these abstract structures into intuitive and understandable geometric representations.

The purpose of this study is to comprehensively examine the Kamada-Kawai algorithm [4], a fundamental and powerful data visualization algorithm that researchers and analysts working with graph data can frequently utilize.

The question of what constitutes a "good" graph drawing has been defined by "aesthetic criteria" in the field of graph drawing. Among these, the most widely accepted criteria are: minimizing the number of edge crossings, visually reflecting the inherent symmetries of the graph, and distributing nodes evenly in the drawing area. The Kamada-Kawai algorithm excels particularly in "reflecting graph-theoretic distance" and "preserving symmetry."

## 2. Fundamentals of the Kamada-Kawai Algorithm

The algorithm, introduced by Tomihisa Kamada and Satoru Kawai in 1989 [4], diverges from other force-directed methods with a fundamental philosophy. While most methods apply attractive forces only between adjacent nodes (local interactions), the KK algorithm aims to preserve the global structure of the graph.

The basic principle of the algorithm is: In a graph drawing, the geometric (Euclidean) distance between any two nodes  $(i, j)$  should be proportional to the graph-theoretic shortest path distance  $(d_{ij})$  between them.

### 2.1. Mathematical Model: The Energy Function

To model this principle, the KK algorithm defines an energy function that aims to minimize the total potential energy (or stress) of the system:

$$E = \sum_{i < j} \frac{1}{2} k_{ij} (|p_i - p_j| - l_{ij})^2$$

The components in this formula are:

- $p_i$  and  $p_j$ : The position vectors of nodes  $i$  and  $j$  in 2D or 3D space.
- $l_{ij}$  (Ideal Distance): The "ideal" spring length between the nodes.  
 $l_{ij} = L \times d_{ij}$  (where  $d_{ij}$  is the shortest path distance between  $i$  and  $j$ ).
- $k_{ij}$  (Spring Stiffness): Determines the stiffness of the spring.  $k_{ij} = K / d_{ij}^2$ .

This model makes the springs between nodes that are "close" on the graph (short shortest path) much stiffer. This means the algorithm is forced to position local structures correctly first, but it does so while considering the global positions of all other nodes.

## 2.2. Algorithm Steps

- **Pre-computation (Most Expensive Step):** The shortest path distances ( $d_{ij}$ ) between  $\textit{all}$  pairs of nodes ( $i, j$ ) in the graph are calculated (Usually with Floyd-Warshall or multiple BFS).
- **Calculation of Ideal Distances:** The  $l_{ij}$  and  $k_{ij}$  values are calculated for all pairs.
- **Initialization:** Nodes are assigned to random positions ( $p_i$ ).
- **Iterative Refinement:** Until the system energy  $E$  falls below a certain threshold, the node causing the most "imbalance" in the system is found, and its position is moved to a new position that locally minimizes the energy using the Newton-Raphson method.

## 3. Application Areas

Kamada-Kawai's ability to preserve global structure and symmetry has made it a valuable tool in many disciplines.

### 3.1. Social Network Analysis (SNA)

In social networks [5], nodes represent individuals, and edges represent relationships (friendship, collaboration, communication). The KK algorithm is invaluable here because:

- **Community Detection:** It visually groups together clusters (cliques) that are in dense communication with each other.
- **Centrality and Bridges:** It places "influential" individuals at the center of the network (those with a low average shortest path) in the center of the

drawing. "Bridge" (broker) individuals who connect different clusters are positioned strategically between these clusters.

### **3.2. Bioinformatics and Systems Biology**

Biological systems, such as protein-protein interaction (PPI) networks or gene regulation networks, are often complex and modular. For these structures, often studied in chemical graph theory [6], KK helps biologists discover functional relationships by visually clustering groups of proteins with similar functional tasks (modules or complexes).

### **3.3. Software Engineering and Database Modeling**

In large-scale software projects, inter-class dependencies, function call graphs, or database schemas (Entity-Relationship diagrams) can be modeled as graphs. KK facilitates the understanding of software architecture by grouping tightly coupled modules (high cohesion) and clearly separating loose connections (low coupling) between different modules.

## **4. Case Study: Social Network Analysis (SNA)**

To demonstrate the power of Kamada-Kawai, let's create a randomized "small-world" graph that models a hypothetical email communication network in an organization of 50 people in Figure 1. Such graphs reflect the high clustering (people often form friend groups) and short average path lengths (everyone is reachable in a few steps) characteristic of social networks.

## 50-Person Social Network Case Study with Kamada-Kawai

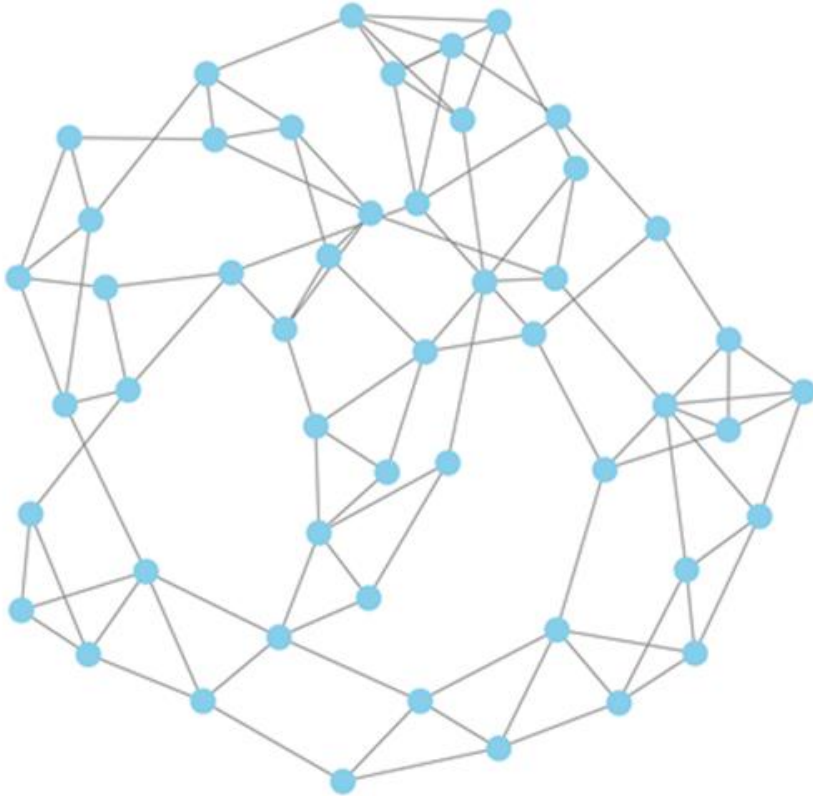


Figure 1: Small-World

### 4.1. Step 1: Generating Randomized Data (Graph)

Let's use the `networkx` library in Python to create a `watts_strogatz_graph` with 50 nodes (employees), where each node has an average of 4 neighbors (close colleagues) and a 0.1 probability of forming new random connections (acquaintances from other departments).

#### PyCode:

```
import networkx as nx
import matplotlib.pyplot as plt
# 1. Case Study Graph: 50 employees, 4 close contacts on average, 10% random links
N = 50
K = 4
P = 0.1
G_sna = nx.watts_strogatz_graph(n=N, k=K, p=P, seed=42)
print(f"Graph Created: {len(G_sna.nodes)} Nodes, {len(G_sna.edges)} Edges")
# 2. Calculate Layout: Kamada-Kawai
print("Calculating Kamada-Kawai layout...")
pos_sna = nx.kamada_kawai_layout(G_sna)
print("Layout complete.")
```

### 4.2. Step 2: Visualization and Analysis

Let's assume we are drawing this `pos_sna` layout. This code has been updated to be clearly visible on an A4 printout.

#### PyCode:

```
# 3. Draw the Graph
plt.figure(figsize=(10, 10), dpi=200)
node_size_updated = 200
nx.draw_networkx(G_sna, pos_sna,
                 node_size=node_size_updated,
                 node_color='skyblue',
                 edge_color='gray',
                 with_labels=False,
                 font_size=12) # Font size increased in case labels are used
# Title
plt.title("50-Person Social Network Case Study with Kamada-Kawai", fontsize=16)
plt.axis('off')
plt.show()
```

### 4.3. Case Analysis (Interpretation of Results)

What does the Kamada-Kawai layout show us?

- **Local Clusters:** Local groups created with the `k=4` parameter (e.g., people in the same department) are visually clustered closely together. KK clearly separates these clusters.
- **Central Actors:** Nodes that are central to the overall communication of the network (those with the lowest average shortest path) are pulled towards the center of the entire drawing. These are the "key" or "most connected" employees in the organization.

- **Bridges (Brokers):** Random connections formed with the  $p=0.1$  probability create "bridges" connecting different clusters. In the KK layout, these nodes are positioned between two or more clusters, connecting them. This is much more understandable than the "hairball" effect that algorithms focusing only on local forces, like Fruchterman-Reingold [7], would produce.

## 5. Performance on Special Graph Topologies

The KK algorithm's goal of preserving global structure makes it an ideal visualization tool, especially for symmetric or complex structures. In this section, the performance of the KK algorithm is demonstrated with Python code using the custom functions you provided for Polygonal Cycle Graphs [8,9] and Dendrimer Graphs [6,10] in Figure 2.

The code block below creates these two special graph structures and, for comparison, Tree/Lattice structures, calculates the Kamada-Kawai layout for each, and visualizes the results in a 2x2 panel with high-resolution and larger vertices.

### PyCode:

```
import networkx as nx
import matplotlib.pyplot as plt
import math
import warnings
warnings.filterwarnings("ignore", category=UserWarning)
# --- Helper Function 1: Polygonal Cycle Graph ---
# (With reference to Sarp et al. [8,9])
def polygonal_cycle_graph(m, n):
    """Generates the polygonal cycle graph for the nth m-gonal number. """
    def P_m(k):
        return k * ((m - 2) * k - m + 4) // 2
    V = list(range(1, P_m(n) + 1))
    G = nx.Graph()
    G.add_nodes_from(V)
    if n == 1:
        return G

    for i in V:
        # Add edge for nodes not equal to P_m(j)
        if i > 1 and i < P_m(n) and not any(P_m(j) == i for j in range(2, n + 1)):
            G.add_edge(i, i + 1)
    # Add edge between P_m(i) and P_m(i+1)
    for i in range(1, n):
        G.add_edge(P_m(i), P_m(i + 1))
    # Add edge between (P_m(i-1) + 1) and (P_m(i) + 1)
```

```

# P_m(0) = 0 for n > 1
for i in range(1, n):
    start_node = P_m(i - 1) + 1
    end_node = P_m(i) + 1
    if end_node <= P_m(n): # Stay within the graph boundaries
        G.add_edge(start_node, end_node)
return G
# --- Helper Function 2: Dendrimer Graph (Gamma Graph) ---
# (With reference to Trinajstić [6] and Bulut & Akar [10])
def create_gamma_graph(n, k, p, h):
    G = nx.Graph()
    # 1. Create the central C_n core
    core_nodes = [f'C_{i}' for i in range(n)]
    G.add_nodes_from(core_nodes)
    for i in range(n):
        G.add_edge(core_nodes[i], core_nodes[(i + 1) % n])
    # Determine core attachment points
    if n >= 6:
        attachment_points_indices = [0, math.floor(n/3), math.floor(2*n/3)]
    elif n == 5:
        attachment_points_indices = [0, 1, 3]
    elif n == 4:
        attachment_points_indices = [0, 1, 2]
    else: # n=3
        attachment_points_indices = [0, 1, 2]
    core_attachment_nodes = [core_nodes[i] for i in attachment_points_indices]
    current_generation_branches = []
    # 2. Add initial arms (Generation 0 branches)
    for i, core_node in enumerate(core_attachment_nodes):
        current_node = core_node
        for j in range(k):
            spacer_node = f'S_{i}_{j}_g0'
            G.add_node(spacer_node)
            G.add_edge(current_node, spacer_node)
            current_node = spacer_node
        current_generation_branches.append(current_node)
    # 3. Iteratively add subsequent generations (h >= 1)
    for gen in range(1, h + 1):
        next_generation_branches = []
        branch_counter = 0
        for parent_node in current_generation_branches:
            for branch_idx in range(p):
                current_node = parent_node
                for j in range(k):
                    new_spacer_node = f'S_{gen}_{branch_counter}_{branch_idx}_{j}'
                    G.add_node(new_spacer_node)
                    G.add_edge(current_node, new_spacer_node)

```

```

        current_node = new_spacer_node
        next_generation_branches.append(current_node)
        branch_counter += 1
        current_generation_branches = next_generation_branches
    return G
# --- 1. Step: Create Graphs ---
print("Generating graphs for special topologies...")
# Graph 1: Polygonal Cycle (m=3, n=6) -> 3-gon (triangle), 6th level
G_pc = polygonal_cycle_graph(m=3, n=6)
# Graph 2: Dendrimer ( $\Gamma_{\{6,2,3,1\}}$ ) -> n=6, k=2, p=3, h=1
G_dend = create_gamma_graph(n=6, k=2, p=3, h=1)
# Graph 3: Balanced Tree (3 branches, 3 levels)
G_tree = nx.balanced_tree(r=3, h=3)
# Graph 4: Grid/Lattice Graph (8x8)
G_grid = nx.grid_2d_graph(m=8, n=8)
# --- 2. Step: Calculate Kamada-Kawai Layouts ---
print("Calculating Kamada-Kawai layouts...")
pos_pc = nx.kamada_kawai_layout(G_pc)
pos_dend = nx.kamada_kawai_layout(G_dend)
pos_tree = nx.kamada_kawai_layout(G_tree)
pos_grid = nx.kamada_kawai_layout(G_grid)
print("All layouts calculated.")

# --- 3. Step: Draw 4 Graphs in 2x2 Subplots ---
# High resolution dpi=250 (suitable for A4)
fig, axs = plt.subplots(2, 2, figsize=(12, 12), dpi=250)
node_size_large = 100

# Subplot title
subplot_title_fontsize = 14
main_title_fontsize = 18

# Graph 1: Polygonal Cycle
axs[0, 0].set_title('Polygonal Cycle Graph (m=3, n=6)', fontsize=subplot_title_fontsize)
nx.draw_networkx(G_pc, pos_pc, ax=axs[0, 0], node_size=node_size_large,
node_color='purple', with_labels=False)
axs[0, 0].axis('off')

# Graph 2: Dendrimer
axs[0, 1].set_title(r'Dendrimer  $\Gamma_{\{6,2,3,1\}}$  (n=6, k=2, p=3, h=1)',
fontsize=subplot_title_fontsize)
nx.draw_networkx(G_dend, pos_dend, ax=axs[0, 1], node_size=node_size_large,
node_color='orange', with_labels=False)
axs[0, 1].axis('off')

# Graph 3: Tree
axs[1, 0].set_title('Balanced Tree (r=3, h=3)', fontsize=subplot_title_fontsize)

```

```

nx.draw_networkx(G_tree, pos_tree, ax=axes[1, 0], node_size=node_size_large,
node_color='green', with_labels=False)
axes[1, 0].axis('off')

# Graph 4: Grid/Lattice
axes[1, 1].set_title('Grid/Lattice Graph (8x8)', fontsize=subplot_title_fontsize)
nx.draw_networkx(G_grid, pos_grid, ax=axes[1, 1], node_size=node_size_large,
node_color='red', with_labels=False)
axes[1, 1].axis('off')

plt.suptitle("Performance of Kamada-Kawai Algorithm on Special Graph Topologies",
fontsize=main_title_fontsize)
plt.tight_layout(rect=[0, 0.03, 1, 0.95])
plt.show()

```

Performance of Kamada-Kawai Algorithm on Special Graph Topologies

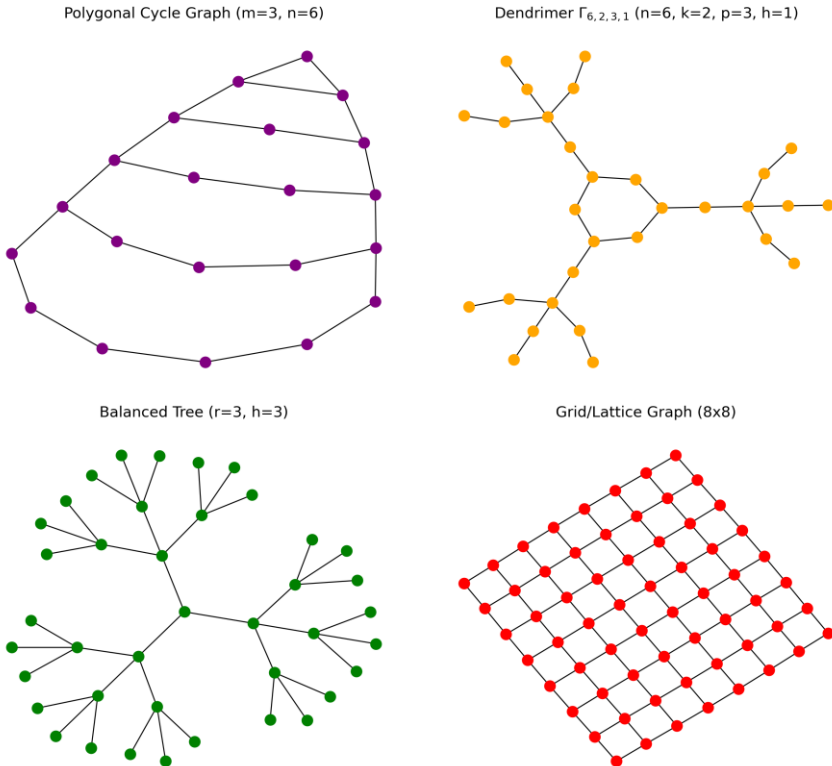


Figure 2: Performance on Special Graph

## 5.1. Interpretation of Code Results

When the code above is executed, the characteristic behavior of the Kamada-Kawai algorithm on these different structures is observed:

**Polygonal Cycle Graph:** KK recognizes the nested triangle ( $m=3$ ) layers ( $n=6$ ) of the graph produced by the `polygonal_cycle_graph` function [8,9] and visualizes them while preserving the symmetry of these layers.

**Dendrimer Graph ( $\Gamma$ ):** KK places the 6-gon core ( $n=6$ ) of the dendrimer produced by `create_gamma_graph` [6,10] at the center and symmetrically spreads the generations ( $h=1$ ) connected via spacers ( $k=2$ ) to the periphery, perfectly displaying the molecule's hierarchical structure.

**Balanced Tree:** Despite having no root information, KK finds the "center" of the graph (usually nodes near the root) and opens the branches outwards symmetrically.

**Grid/Lattice:** KK recognizes the highly regular structure of the grid graph and reconstructs it into an almost perfect square grid by reflecting the shortest path distances (Manhattan distance) to Euclidean distances.

## 6. Limitations, Challenges, and Modern Approaches

Despite Kamada-Kawai's aesthetic success, it has serious practical challenges.

### 6.1. Limitations and Challenges

**Computational Complexity (The Biggest Limitation):** The first step of the algorithm is to compute the All-Pairs Shortest Path (APSP) matrix. In dense graphs, this takes  $O(|V|^3)$  (Floyd-Warshall) or in sparse graphs  $O(|V| \cdot |E|)$  (BFS from each node) time [11, 12]. This makes the algorithm practically unusable for graphs larger than a few thousand nodes (e.g.,  $V > 2000$ ).

**Local Minima:** The energy minimization process (Newton-Raphson) can get stuck in a "good enough" local minimum instead of the "ideal" global minimum energy state. This can happen, especially when starting from a poor initial position.

### 6.2. Modern Approaches and Improvements

To overcome these limitations, modern graph drawing tools [11, 12] and researchers [13, 14] have developed various strategies:

**Multilevel Approaches:** One of the most effective solutions [13]. Instead of drawing the large graph directly, the algorithm "coarsens" the graph—creating a smaller, representative graph by merging nodes. KK is run quickly on this much

smaller graph. Then, the layout is "*uncoarsened*," and the nodes of the original graph are settled into place with local adjustments.

**Sampling:** To avoid the  $O(|V|^3)$  cost, the entire APSP matrix is not calculated. Instead, a random subset of nodes (landmark nodes) is selected, and distances are approximated based only on these nodes [14].

**Hybrid Approaches:** Used to prevent KK from getting stuck in local minima. The graph is first roughly laid out with a faster algorithm that preserves less global structure, such as Fruchterman-Reingold (FR). This "*good enough*" layout is then used as a starting point for the KK algorithm, which performs the final "polishing."

**GPU and Parallel Computing:** The APSP calculation and the force calculations in energy minimization are inherently parallelizable operations. Modern approaches aim to achieve significant speedups by moving these computations to GPUs.

## 7. Conclusion

The Kamada-Kawai algorithm has been one of the cornerstones of graph drawing literature since its presentation in 1989. Its energy model, based on graph-theoretic distances, produces aesthetically superior drawings that emphasize global structure and symmetry, especially in fields like Social Network Analysis and Bioinformatics.

However, its high computational cost, severely limits the algorithm's direct applicability in the "*big data*" era. Therefore, in modern applications, Kamada-Kawai lives on as a "*refinement*" step, often within Multilevel techniques or hybrid approaches combined with algorithms like Fruchterman-Reingold.

## References

- [1] Diestel, R. (2025). Graph theory (Vol. 173). Springer Nature.
- [2] Gross, J. L., Yellen, J., & Anderson, M. (2018). Graph theory and its applications. Chapman and Hall/CRC.
- [3] West, D. B. (2001). Introduction to graph theory (2nd ed.). Prentice Hall.
- [4] Kamada, T., & Kawai, S. (1989). An algorithm for drawing general undirected graphs. Information processing letters, 31(1), 7-15.
- [5] Susamcıoğlu, L., Alaybeyoğlu, A., & Sarp, Ü. (24-25 April 2025). Geometric Pattern Based Interpretable Link Prediction in Social Networks: GNN Application on Facebook Dataset. 5th International Artificial Intelligence and Data Science Congress (ICADA 2025), Zonguldak, Türkiye.
- [6] Trinajstić, N. (1992). Chemical graph theory (2nd ed.). CRC press.
- [7] Fruchterman, T. M. J., & Reingold, E. M. (1991). Graph drawing by force-directed placement. Software: Practice and Experience, 21(11), 1129-1164.
- [8] Sarp, Ü., Demir, B., & Emin, A. (2025, April 24–25). Visualization and edge intersection analysis of polygonal cycle graphs. 5th International Artificial Intelligence and Data Science Congress (ICADA 2025), Zonguldak, Türkiye.
- [9] Sarp, Ü., Demir, B., Emin, A., & Cangül, I. N. (2025). Introducing a new family of graphs associated to the polygonal numbers: Polygonal cycle graphs. To appear.
- [10] Bulut, M., & Akar, E. (2012). Dendrimerlerin önemi ve kullanım alanları. Teknik Bilimler Dergisi, 2(1), 5–11.
- [11] NetworkX Developers. (2025). kamada\_kawai\_layout. In NetworkX documentation (Version 3.x). Python Software Foundation.
- [12] Graphviz Developers. (2025). Layout algorithms. In Graphviz documentation (Version 9.x). AT&T Research.
- [13] Walshaw, C. (2000, September). A multilevel algorithm for force-directed graph drawing. In International Symposium on Graph Drawing (pp. 171-182). Berlin, Heidelberg: Springer Berlin Heidelberg.
- [14] Hachul, S., & Jünger, M. (2005, September). An experimental comparison of fast algorithms for drawing general large graphs. In International Symposium on Graph Drawing (pp. 235-250). Berlin, Heidelberg: Springer Berlin Heidelberg.